SIP-IFVM: An efficient time-accurate implicit MHD model of corona and CME with strong magnetic field

H. P. Wang[1, 2], J. H. Guo[1, 3], L. P. Yang[2], S. Poedts[1, 4], F. Zhang[5, 6], A. Lani[1, 7], T. Baratashvili[1], L. Linan[1], R. Lin[1, 8], and Y. Guo[3]

[1] Centre for Mathematical Plasma-Astrophysics, Department of Mathematics, KU Leuven, Celestijnenlaan 200B, 3001 Leuven, Belgium
   e-mail: `haopeng.wang1@kuleuven.be`
[2] State Key Laboratory of Space Weather, Chinese Academy of Sciences, Beijing 100190, China
[3] School of Astronomy and Space Science and Key Laboratory of Modern Astronomy and Astrophysics, Nanjing University, Nanjing 210023, China
   e-mail: `jinhan.guo@kuleuven.be`
[4] Institute of Physics, University of Maria Curie-Skłodowska, ul. Radziszewskiego 10, 20-031 Lublin, Poland
   e-mail: `Stefaan.Poedts@kuleuven.be`
[5] Institute of Theoretical Astrophysics, University of Oslo, PO Box 1029 Blindern, 0315 Oslo, Norway
[6] Rosseland Centre for Solar Physics, University of Oslo, PO Box 1029 Blindern, 0315 Oslo, Norway
[7] Von Karman Institute For Fluid Dynamics, Waterloosesteenweg 72, 1640 Sint-Genesius-Rode, Brussels, Belgium
[8] School of Earth and Space Sciences, Peking University, Beijing 100871, China

September 4, 2024

ABSTRACT

Context. Coronal mass ejections (CME) are one of the main drivers of space weather. However, robust and efficient numerical modeling of the initial stages of CME propagation and evolution process in the sub-Alfvénic corona is still lacking.
Aims. Magnetohydrodynamic (MHD) solar coronal models are critical in the Sun-to-Earth model chain but sometimes encounter low-β ($< 10^{-4}$) problems near the solar surface. This paper aims to deal with these low-β problems and make MHD modeling suitable for practical space weather forecasting by developing an efficient and time-accurate MHD model of the solar corona and CME launch. In this paper, we develop an efficient and time-accurate three-dimensional (3D) single-fluid MHD solar coronal model and employ it to simulate the CME's evolution and propagation.
Methods. This model is developed based on the quasi-steady-state implicit MHD coronal model (Feng et al. 2021; Wang et al. 2022a), which can increase computational efficiency by adopting a large time-step size. Furthermore, a pseudo-time marching method, where a pseudo time τ is introduced at each physical time step to update the solution by solving a steady-state problem on τ, is devised to improve the temporal accuracy of CME simulations; a Regularized Biot-Savart Laws (RBSL) flux rope, whose axis can be designed in arbitrary shape, is inserted to the background corona to trigger the CME event. We call this model the Solar Interplanetary Phenomena-Implicit Finite Volume Method (SIP-IFVM) coronal model and utilize it to simulate a CME evolution process from the solar surface to 20 R_s in the background corona of Carrington rotation (CR) 2219. Compared to the explicit model, it can achieve a speedup of over 60 × in quasi-steady-state coronal simulations, with the average relative difference in plasma density, $RD_{\text{ave},\rho}$, being only 3.05%. In CME simulations covering 6 hours of physical time, the computational time is less than 0.5 hours (192 CPU cores, ∼1 M cells) using an appropriate large time-step size. It achieves a speedup of over 6 ×, with $RD_{\text{ave},\rho} < 2.0\%$, compared to the simulation using a small time-step size determined by the Courant-Friedrichs-Lewy (CFL) stability restriction. Additionally, we use this model to conduct an ad hoc simulation by artificially increasing the initial magnetic field strength of the background corona and flux rope, it indicates that the model can efficiently deal with the time-dependent problems with plasma β (the ratio of the thermal pressure to the magnetic pressure) as low as about 5×10^{-4}. We also simulate an Orszag-Tang MHD vortex flow using the pseudo-time-marching method adopted in the SIP-IFVM coronal model, it shows that the pseudo-time-marching method adopted in this model is also capable of simulating small-scale unsteady-state flows.
Results. The simulation results show that this MHD coronal model is very efficient and numerically stable and is promising to timely and accurately simulate time-varying events in solar corona with low plasma β.

Key words. Magnetohydrodynamics (MHD) –methods: numerical –Sun: corona –Sun: coronal mass ejections (CMEs)

1. Introduction

Disastrous space weather is caused by solar storms that propagate to the Earth's orbit and suddenly produce a negative impact on our high-tech space-based and ground-based infrastructure on which our activities depend. The economic losses caused by disastrous space weather to human society are increasing. There is thus an urgent need to understand the mechanism of

space weather and eventually to be able to give reliable forecasts hours to days in advance (e.g., Baker 1998; Feng et al. 2011a, 2013; Feng 2020b; Koskinen et al. 2017; Poedts, S. et al. 2020; Singer et al. 2001; Siscoe 2000). To achieve this goal, we need to develop and improve advanced numerical models to further unravel the complex mechanisms of space weather.

The physically based MHD modeling is the first principal method capable of bridging large heliocentric distances from

near the Sun to well beyond Earth's orbit self-consistently and revealing the fundamental propagation and evolution processes of complex solar storms (e.g., Detman et al. 2006; Dryer 2007; Feng et al. 2007, 2010, 2011b, 2012a,b, 2014a,b, 2017; Feng 2020b; Gombosi et al. 2018; Hayashi et al. 2006a; Li & Feng 2018; Li et al. 2020; Lugaz & Roussev 2011; Mikić et al. 1999; Nakamizo et al. 2009; Riley et al. 2012; Shen et al. 2021; Tóth et al. 2012; Usmanov 1993; Usmanov & Goldstein 2003; Wu & Dryer 2015; Yang et al. 2021; Zhou et al. 2012; Zhou & Feng 2017). However, realistic MHD simulation is a complex process involving disparate physical spatiotemporal scales, and is very computationally intensive. To be able to take appropriate measures in advance to guarantee the regular operation of increasingly frequent high-tech activities of human beings and eventually avoid possible economic losses, we should spare no effort to study and establish efficient, spatiotemporal accurate and numerical stable MHD models and utilize these advanced models to timely and accurately predict severe space weather (e.g., Feng 2020b; Owens et al. 2017, and references therein).

Usually, coupling different models dedicated to specific regions and physical problems is the preferred choice for establishing a space-weather forecasting framework (e.g., Feng et al. 2013; Goodrich et al. 2004; Hayashi et al. 2021; Kuźma et al. 2023; Odstrcil et al. 2004; Perri et al. 2022, 2023; Poedts, S. et al. 2020; Tóth et al. 2012). Among these coupled components, the solar coronal model is crucial for determining the initialization of the remaining models, and is also a key factor affecting the simulation results of solar disturbance propagation and evolution (Brchnelova et al. 2022; Perri et al. 2023). In such solar coronal regions, the solar wind velocity is increased from subsonic to supersonic. Also, the Solar disturbances, such as coronal mass ejections (CMEs) and solar proton events, propagate through the solar coronal region (Feng 2020b; Kuźma et al. 2023).

However, MHD simulations of the solar corona are also the most complex and computationally intensive component and sometimes encounter low β (the ratio of the thermal pressure to the magnetic pressure) problems with β as low as 10^{-4} near the solar surface (Bourdin 2017). For example, to update for 1 hour of real-time needs about 50 hrs of computing time on 100 CPUs in the data-driven MHD modeling of a flux-emerging active region inside the low corona (Jiang et al. 2016). In this simulation, $\beta = 2 \times 10^{-3}$ and the time step size is smaller than 0.1 seconds due to the restriction of Courant-Friedrichs-Lewy (CFL) stability condition. Even a steady-state global solar coronal simulation by an explicit MHD model, which uses a solenoidality-preserving approach to maintain magnetic field divergence-free constraints, takes about 50 hrs of computing time on 576 MPI processes to obtain a steady-state solution (Feng et al. 2019). In this simulation, $\beta = 1 \times 10^{-3}$ near the solar surface, and the time-step size is consequently limited to around 3.6 seconds.

As high efficiency and stability are required in practical applications, compromises are usually made in solar coronal simulations. For instance, empirical Wang-Sheeley-Arge (WSA) (Arge et al. 2003; Yang et al. 2018) solar coronal model in EUHFORIA (Poedts, S. et al. 2020; Pomoell & Poedts 2018), the magneto-frictional (MF) coronal nonlinear force-free fields module in MPI-AMRVAC (Guo et al. 2016), and simplified physical-based zero-β solar coronal model (Caplan et al. 2019) are used to calculate the solar coronal structures roughly. However, these simplifications discard a lot of important information, and it was demonstrated that a simple MHD model provides better forecasts than an empirical solar coronal model (Samara et al.

2021). Therefore, many researchers are devoted to establishing more efficient and accurate MHD solar coronal models (Feng 2020b; Kuźma et al. 2023). In such cases, we should develop advanced MHD coronal models with high precision, strong numerical stability, and fast computational efficiency to reconstruct complex coronal structures accurately and timely to improve our space weather forecasting ability.

Recently, Feng et al. (2021) and Wang et al. (2022a,b) have established a series of 2nd-order accurate, efficient, and robust implicit MHD solar coronal models capable of dealing with low-β problems. They reduce the wall-clock times of steady-state MHD solar coronal simulations from several days to less than 1 hour under the same computing environment. However, these steady-state models still have a lot of room to be improved in spatiotemporal resolution. In this paper, we further carry out some research work on developing both a time-accurate and numerical stable implicit MHD solar coronal model and call it the SIP-IFVM (Solar-Interplanetary Phenomena-Implicit Finite Volume Method) coronal model. This SIP-IFVM coronal model is employed to simulate the evolution and propagation procedure of CMEs in background coronas. Based on the research work presented in this paper, we will further develop spatiotemporal high-order accurate and computationally efficient implicit MHD solar coronal models in our subsequent research works.

In the implicit algorithm, although the convergence rate can be improved by selecting a considerable time step (Brchnelova et al. 2023; Feng et al. 2021; Kuźma et al. 2023; Liu et al. 2023; Perri et al. 2022, 2023; Wang et al. 2019, 2022a,b), it may be accompanied by a loss in temporal accuracy (Linan et al. 2023). By mimicking the evolution and propagation of flux ropes, it was proved that the implicit solar coronal model can be time-accurate and still faster than the explicit MHD model by selecting a suitable time step size (Guo et al. 2023; Linan et al. 2023). Besides, some researchers employed the pseudo-time marching method by introducing a pseudo time τ at each physical time step and solving a steady-state problem on τ to guarantee the temporal accuracy (e.g. Bijl et al. 2002; Li et al. 2019; Luo et al. 2001; Sitaraman & Raja 2013). However, the rough selection of a small time step and pseudo-time marching method can reduce computation efficiency. To make the time-accurate simulation more efficient, some flexible time-step size adaption strategies (Hoshyari et al. 2020; Noventa et al. 2020) are proposed and implemented in fluid dynamics simulations of both steady and unsteady flows. In this paper, we first employ the implicit MHD model with a considerable time step to mimic the steady-state coronal structures, and then select a relatively small time step and carry out the pseudo-time marching method at each physical time step to guarantee both the computation efficiency and the necessary accuracy of the CME simulations.

After establishing this efficient time-accurate coronal model capable of dealing with low β problems, we carried out some CME simulations to further validate the model's capability of mimicking the propagation and evolution processes of CMEs. Generally, two kinds of models exist to initiate a CME in a numerical space-weather framework. The first one is based on the non-magnetic hydrodynamic cloud, such as the plasmasphere cone model (Hayashi et al. 2006b; Mays et al. 2015; Odstrcil & Pizzo 1999; Pomoell & Poedts 2018; Zhao et al. 2002). This model can roughly retrieve the geometry and dynamics of CMEs, i.e., the angular width, ejection direction, and propagation speed. Therefore, this model is generally used to predict the arrival time of CMEs and the intensity of their induced shock. However, observations suggest that most CMEs

include a magnetic flux rope. For instance, filaments (Guo et al. 2021; Ouyang et al. 2017) and hot channels (Cheng et al. 2017; Zhang et al. 2012) are often found to be progenitors of CMEs, which are frequently served as the proxies of magnetic flux ropes in observations. Many non-linear-force-free-field extrapolation and data-driven models also demonstrate the existence of pre-eruptive flux ropes (Cheung & DeRosa 2012; Guo et al. 2017; Pomoell & Poedts 2018). Furthermore, observations of white-light coronagraph observations found that almost one-half of the CMEs manifest a twisted flux rope structure (Vourlidas et al. 2012). In addition, some in-situ detections in interplanetary space found that CMEs usually hold a monotonic rotation of internal magnetic fields, indicating the twisted flux-rope field lines (Burlaga et al. 1981). As a result, constrained by these observations, it seems that magnetic flux rope-based CME-initialization models are more realistic.

In recent decades, many magnetic flux rope models used to initiate a CME have been proposed. However, torus-shaped and cylindrical flux rope models are widely used to initialize CME simulations (Kataoka et al. 2009; Marubashi et al. 2016; Nieves-Chinchilla et al. 2018; Singh et al. 2020; Scolini, C. et al. 2019; Yang et al. 2021; Zhang et al. 2019; Zhou & Feng 2017). Such as the Gibson–Low flux rope model (Gibson & Low 1998) adopted in AWSoM (Jin et al. 2017). AWSoM is a data-driven model with a domain extending from the upper chromosphere to the corona and heliosphere which has been implemented in the Space Weather Modeling Framework (Tóth et al. 2012). Also, some analytical modified Titov-Démoulin circular (Titov et al. 2014) and an S-shaped regularized Biot-Savart laws (Titov et al. 2017) flux ropes have been implemented in COCONUT (COolfluid COroNal UnsTructured) coronal model (Guo et al. 2023; Linan et al. 2023), MAS code (Linker et al. 2024), PLUTO code (Regnault et al. 2023) and MPI-AMRVAC (Guo et al. 2019; Keppens et al. 2023). COCONUT is one of the rapidly developing MHD models with an implicit temporal integration method (Brchnelova et al. 2022, 2023; Kuźma et al. 2023; Perri et al. 2022, 2023), MAS is one of the currently most matured and advanced solar coronal models and adopt a semi-implicit operator (Caplan et al. 2019), PLUTO is a multi-physics and multi-solver explicit MHD code (Mignone et al. 2011), and MPI-AMRVAC is an open-source framework for parallel, grid-adaptive simulations of hydrodynamic and MHD astrophysical applications (Xia et al. 2018). In this paper, we further adopt the RBSL flux rope, which allows an arbitrary shape of the electric current path, to initialize CME simulations in a very numerical stable, efficient, and time-accurate implicit thermodynamic MHD coronal model. What makes this SIP-IFVM model different from the aforementioned coronal models is mainly its adoption of the parallel LU-SGS matrix solver, the pseudo-time marching method, the approximate linearization strategy, the decomposed MHD equation, and the six-component grid system described below. These combined features significantly enhance the efficiency, time accuracy, and numerical stability of the coronal model.

Firstly, we mimic a CME evolution and propagation process driven by an RBFL flux rope with a theoretical "S"-shape curve path to validate the novel algorithms proposed in this paper. Secondly, we demonstrate the model's capability of mimicking a robust magnetic environment by using this model to conduct an ad hoc simulation with the initial magnetic field of the background corona and flux rope multiplied by 5 and 2.5, respectively. Finally, we perform an Orszag-Tang MHD vortex flow simulation (Orszag & Tang 1979) to show that the novel pseudo-time marching method adopted in this paper is capable of simulat-

ing small-scale unsteady-state flows, so does this MHD coronal model. Considering that CME is one of the main drivers of space weather (Vourlidas et al. 2019; Zhang et al. 2023), but there is still a lack of robust and efficient modeling of the initial stages of CME propagation and shock evolution in the sub-Alfvénic corona below about $20\,R_s$ (Vourlidas et al. 2019), the novel coronal model developed in this paper is precisely what is needed and expected to play an active role in improving our space weather forecasting capabilities.

Based on the above considerations, the paper is organized as follows. In Section 2, we introduce the governing equations and grid system for the solar coronal and CME simulations and demonstrate the RBSL flux rope-based CME initialization. In Section 3, the numerical formulation of the MHD coronal model is described in detail. This section mainly describes the discretization of the decomposed MHD equations, the implementation of the pseudo-time marching method, and the processing of boundary conditions. We demonstrate the simulation results in Section 4 and Appendix A. In Section 5, we summarize the main features of the efficient time-accurate implicit MHD coronal model and give some concluding remarks.

2. Governing equations and initialization

This section mainly describes the governing equations and initialization of the steady-state background coronal and time-varying CME simulations.

2.1. The governing equations

In this paper, based on the implicit MHD quasi-steady-state coronal model (Feng et al. 2021; Wang et al. 2022a,b), we further develop an efficient time-accurate MHD model of corona and CME.

We solve the decomposed MHD equations, where the magnetic field $\mathbf{B} = \left(B_x, B_y, B_z\right)^T$ is split into a time-independent potential magnetic field $\mathbf{B}_0 = \left(B_{0x}, B_{0y}, B_{0z}\right)^T$ and a time-dependent field $\mathbf{B}_1 = \left(B_{1x}, B_{1y}, B_{1z}\right)^T$ (e.g., Feng et al. 2010; Fuchs et al. 2010; Guo 2015; Ogino & Walker 1984; Powell et al. 1999; Tanaka 1995; Wang et al. 2022a). The governing MHD equations are calculated in the heliographic rotating coordinate system (Fränz & Harper 2002; Thompson 2006), and reads as follows (Wang et al. 2022a).

$$
\begin{cases}
\frac{\partial \rho}{\partial t} + \nabla \cdot (\rho \mathbf{v}) = 0, \\
\frac{\partial (\rho \mathbf{v})}{\partial t} + \nabla \cdot \left[\rho \mathbf{v}\mathbf{v} + \left(p + \frac{\mathbf{B}_1^2}{2} + \mathbf{B}_1 \cdot \mathbf{B}_0 \right)\mathbf{I} - \mathbf{B}_1\mathbf{B}_1 - \mathbf{B}_1\mathbf{B}_0 - \mathbf{B}_0\mathbf{B}_1 \right] \\
\quad = -(\nabla \cdot \mathbf{B}_1)\mathbf{B} - \frac{\rho G M_s}{r^3}\mathbf{r} - 2\rho\boldsymbol{\omega} \times \mathbf{v} - \rho\boldsymbol{\omega} \times (\boldsymbol{\omega} \times \mathbf{r}) + \mathbf{S}_m, \\
\frac{\partial E_1}{\partial t} + \nabla \cdot \left[(E_1 + p_{T1} + \mathbf{B}_1 \cdot \mathbf{B}_0)\mathbf{v} - \mathbf{B}(\mathbf{v} \cdot \mathbf{B}_1) \right] \\
\quad = -(\nabla \cdot \mathbf{B}_1)(\mathbf{v} \cdot \mathbf{B}_1) - \rho\mathbf{v} \cdot \left(\frac{GM_s}{r^3}\mathbf{r} + \boldsymbol{\omega} \times (\boldsymbol{\omega} \times \mathbf{r}) \right) + S_E, \\
\frac{\partial \mathbf{B}_1}{\partial t} + \nabla \cdot (\mathbf{v}\mathbf{B} - \mathbf{B}\mathbf{v}) = -(\nabla \cdot \mathbf{B}_1)\mathbf{v}.
\end{cases}
\tag{1}
$$

In this equation, $\mathbf{B} = \mathbf{B}_0 + \mathbf{B}_1$, $E_1 = \frac{p}{\gamma - 1} + \frac{1}{2}\rho\mathbf{v}^2 + \frac{1}{2}\mathbf{B}_1^2$ and $p_{T1} = p + \frac{\mathbf{B}_1^2}{2}$. In the solar coronal model, the polytropic index is set to $\gamma = 1.05$ (Hayashi et al. 2006a; Linker et al. 1999; Steinolfson & Hundhausen 1988; Wu et al. 1999; Wu & Dryer 2015). In the definition of the magnetic field, a factor of $\frac{1}{\sqrt{\mu_0}}$ is absorbed with $\mu_0 = 4 \times 10^{-7}\pi$ H m^{-1} denoting the magnetic permeability. ρ and $\mathbf{v} = (u, v, w)^T$ represent the plasma

density and the velocity in the Cartesian coordinate system. As usual, G means the universal gravitational constant, M_s means the mass of the Sun, and GM_s is 1.327927×10^{20} m^3 s^{-2}. Also, $|\omega| = \frac{2\pi}{25.38}$ radian day^{-1} denotes the sidereal angular speed of the Sun (Priest 2014), $\mathbf{r}$ is the position vector and $r = |\mathbf{r}|$ denotes the heliocentric distance. The thermal pressure of the plasma is defined as $p = \Re\rho T$, where $\Re = 1.653 \times 10^4$ m^2 s^{-2} K^{-1} denotes the gas constant, and T is the temperature of the bulk plasma.

For convenience of description, we write the above MHD equations in the following compact form

$$\frac{\partial \mathbf{U}}{\partial t} + \nabla \cdot \mathbf{F}(\mathbf{U}) = \frac{\partial \mathbf{U}}{\partial t} + \frac{\partial \mathbf{f}(\mathbf{U})}{\partial x} + \frac{\partial \mathbf{g}(\mathbf{U})}{\partial y} + \frac{\partial \mathbf{h}(\mathbf{U})}{\partial z} = \mathbf{S}(\mathbf{U}, \nabla\mathbf{U}). \quad (2)$$

Here, $\mathbf{U} = (\rho, \rho\mathbf{v}, E_1, \mathbf{B}_1)^T$ denotes the conservative variable vector, $\nabla\mathbf{U}$ corresponds to the derivative of $\mathbf{U}$, $\mathbf{F}(\mathbf{U}) = (\mathbf{f}, \mathbf{g}, \mathbf{h})$ is the flux vectors in the x, y and z directions, and $\mathbf{S} = \mathbf{S}_{\text{Powell}} + \mathbf{S}_{\text{gra}} + \mathbf{S}_{\text{rot}} + \mathbf{S}_{\text{heat}}$ represents the source term vector corresponding to the Godunov-Powell source terms, the gravitational force, the Coriolis force, and the heating source terms defined as below

$$
\begin{aligned}
\mathbf{S}_{\text{Powell}} &= -\nabla \cdot \mathbf{B}_1 \begin{pmatrix} 0 \\ \mathbf{B} \\ \mathbf{v} \cdot \mathbf{B}_1 \\ \mathbf{v} \end{pmatrix}, \\
\mathbf{S}_{\text{gra}} &= -\frac{\rho GM_s}{|\mathbf{r}|^3} \begin{pmatrix} 0 \\ \mathbf{r} \\ \mathbf{r} \cdot \mathbf{v} \\ \mathbf{0} \end{pmatrix}, \\
\mathbf{S}_{\text{rot}} &= -\rho \begin{pmatrix} 0 \\ \omega \times (\omega \times \mathbf{r}) + 2\omega \times \mathbf{v} \\ \mathbf{v} \cdot (\omega \times (\omega \times \mathbf{r})) \\ \mathbf{0} \end{pmatrix}, \\
\mathbf{S}_{\text{heat}} &= -\begin{pmatrix} 0 \\ \mathbf{S}_m \\ S_E \\ \mathbf{0} \end{pmatrix}.
\end{aligned}
\quad (3)
$$

The term $\mathbf{S}_{\text{heat}}$ is used to mimic the effect of coronal heating and solar wind acceleration (e.g., Feng et al. 2010; Li et al. 2005; Lionello et al. 2008; Riley et al. 2015; Suess et al. 1996). In definition of $\mathbf{S}_{\text{heat}}$, $\mathbf{S}_m$ denotes the momentum source term vector, and $S_E = Q_e + \mathbf{v} \cdot \mathbf{S}_m + \nabla \cdot \mathbf{q}$ is the energy source term. $\mathbf{S}_m$ and S_E are defined the same as in Wang et al. (2022a), with Q_e being the volumetric heating function and $\nabla \cdot \mathbf{q}$ the thermal conductivity term. The heat flux $\mathbf{q}$ is defined in a Spitzer form or collisionless form according to the radial distance (Hollweg 1978) as below

$$\mathbf{q} = \begin{cases} \xi T^{5/2}(\hat{\mathbf{b}} \cdot \nabla T)\hat{\mathbf{b}}, & \text{if } 1 \le r \le 10R_s \\ -\alpha n_e k_B T\mathbf{v}, & \text{if } r > 10R_s \end{cases}. \quad (4)$$

Here, $\hat{\mathbf{b}} = \frac{\mathbf{B}}{|\mathbf{B}|}$, $\xi = 1.6 \times 10^{-12}$ J m^{-1} s^{-1} K$^{-\frac{7}{2}}$ (Endeve et al. 2003; Feng et al. 2010), α is set to 1 (Lionello et al. 2008), n_e is the electron number density, and $k_B = 1.380649 \times 10^{-23}$ J K^{-1} means the Boltzmann constant.

The governing equations described above are used to conduct simulations for the steady-state background solar corona and the evolution and propagation of CMEs. First, we perform a time-relaxation procedure to achieve a quasi-steady background corona. When the steady-state simulation converges, we add the flux rope magnetic field to $\mathbf{B}_1$ of the quasi-steady background corona and then carry out the subsequent time-accurate CME simulation.

In the background coronal simulation, the time variable t in Eq. (2) doesn't refer to a physical time but a relaxation time used to implement the time-relaxation iteration to get a quasi-steady state coronal structure. As for the time-dependent CME simulation, we must maintain the implicit algorithm's temporal accuracy where the physical time-step size exceeds the CFL stability restriction. In this paper, we introduce a pseudo time τ to Eq. (2) as below and update the solution variables for the CME simulations on physical time t by solving a steady-state problem on τ:

$$\frac{\partial \mathbf{U}}{\partial \tau} + \left(\frac{\partial \mathbf{U}}{\partial t} + \mathbf{R}(\mathbf{U}, \nabla\mathbf{U})\right) = \mathbf{0} \quad (5)$$

where $\mathbf{R}(\mathbf{U}, \nabla\mathbf{U}) = \nabla \cdot \mathbf{F}(\mathbf{U}) - \mathbf{S}(\mathbf{U}, \nabla\mathbf{U})$. More description of how to solve Eq. (5) is presented in Subsection 3.3.

To make the governing equations more convenient to discretize, the variables $\mathbf{r}$, ρ, $\mathbf{v}$, p, $\mathbf{B}$, t and ω are normalized by R_s (solar radius), ρ_s, a_s, $\rho_s a_s^2$, $\sqrt{\rho_s a_s^2}$, $\frac{R_s}{a_s}$ and $\frac{a_s}{R_s}$, respectively. Here, ρ_s and a_s denote the plasma density and the acoustic wave speed at the solar surface.

2.2. Initialization of quasi-steady coronal and time-varying CME simulations

The observed synoptic magnetogram of the photosphere constrains the steady-state simulation of the background corona. The radial magnetic field at the inner boundary is obtained from the line-of-sight photospheric magnetic data provided by the GONG-ADAPT (Global Oscillation Network Group-Air Force Data Assimilative Photospheric Flux Transport) magnetogram (Li et al. 2021; Perri et al. 2023). At the beginning of the steady-state solar coronal simulations, the magnetic field $\mathbf{B}_0$ is generated from the potential field (PF) solver of 20-order spherical harmonic expansion, and the magnetic field topology information contained in the definition of the volumetric heating function Q_e is derived from the magnetic field calculated from the potential field source surface (PFSS) model (e.g., Arge et al. 2004; Ljubomir & Larisa 2012; Newkirk et al. 1970; Reiss et al. 2019; Schatten et al. 1969). The PF and PFSS models adopt the observed GONG-ADAPT photospheric magnetogram as the inner boundary. As usual, the plasma density ρ, radial speed v_r and thermal pressure p are given by solving Parker's one-dimensional hydrodynamic isothermal solar wind solution (Parker 1963) and the initial temperature and proton number density at the solar surface are set to be 1.3×10^6K and 1.5×10^8cm^{-3}, respectively.

After the quasi-steady coronal simulation converged, the magnetic field of the RBSL flux-rope is superposed to the quasi-steady corona by implementing a divergence-free RBF (radial basic function) interpolation (Wang et al. 2022a) to initialize the CME simulations. In this paper, the grid of the RBSL flux rope model is treated as a spherical mesh of $(1R_s \le r \le 3R_s) \times \left(\theta_{FR} - \frac{\pi}{4} \le \theta \le \theta_{FR} + \frac{\pi}{4}\right) \times \left(\phi_{FR} - \frac{\pi}{2} \le \phi \le \phi_{FR} + \frac{\pi}{2}\right)$ with θ_{FR} and ϕ_{FR} determined by the value of θ and ϕ of the flux-rope axis path's central point. The grid mesh distributes uniformly along θ- and ϕ- directions with a resolution of 160×320 and coincident with the coronal mesh in the radial direction. Titov et al. (2017) proposed the RBSL model to construct a flux rope with an arbitrary path for its axis. It effectively reconstructs the magnetic structures of CME progenitors and models their initiation and propagation in the heliosphere (Guo et al. 2019; Guo et al. 2021, 2023). In the following text of this subsection, we briefly introduce the configuration of the RBSL flux rope utilized to initialize CME simulations in our SIP-IFVM coronal model.

In the RBSL flux rope model, the magnetic field at a position $\mathbf{x}$ and denoted by $\mathbf{B}_{FR}(\mathbf{x})$ is calculated as the curl of an axial vector potential field and an azimuthal vector potential field,

$$\mathbf{B}_{FR}(\mathbf{x}) = \nabla \times \mathbf{A}_I(\mathbf{x}) + \nabla \times \mathbf{A}_F(\mathbf{x})$$

$$\begin{cases} \mathbf{A}_I(\mathbf{x}) = \frac{\mu_0 I}{4\pi} \oint_{C \cup C^*} K_I(r) \mathbf{R}'(l) \frac{dl}{a(l)} \\ \mathbf{A}_F(\mathbf{x}) = \frac{F}{4\pi} \oint_{C \cup C^*} K_F(r) \mathbf{R}'(l) \times \mathbf{r} \frac{dl}{a(l)^2} \end{cases} \quad . \quad (6)$$

It is assumed that the axial vector potential field $\mathbf{A}_I(\mathbf{x})$ and its curl $\nabla \times \mathbf{A}_I$, the azimuthal magnetic field, is generated by a current I. The azimuthal vector potential field $\mathbf{A}_F(\mathbf{x})$ and its curl $\nabla \times \mathbf{A}_F$, the axial magnetic field, are generated by a net flux F (Titov et al. 2017). Here C is the axis path of the flux rope, C^* is chosen as a mirror image of C concerning the smallest circular section passing through the two intersections of C and solar surface, l and $a(l)$ denote the arc length and cross-sectional radius of axis path respectively, and $K_I(r)$ and $K_F(r)$ are kernels of the RBSL flux rope. For convenience of calculation, $a(l)$ is simplified to a constant variable $a(l) \equiv a = \text{const}$ along the flux rope. In addition, the current I and flux F meet the following relationship

$$F = \pm \frac{3\mu_0 I a}{5\sqrt{2}}, \quad (7)$$

with the sign determined by the helicity of the flux rope. The RBSL flux rope can be defined by the flux F, axis path C, and cross-sectional radius a. A more detailed description of the RBSL flux rope model can be found in Titov et al. (2017) and Guo et al. (2023). In this paper, we adopt a theoretical curve path to confine the axis path of the RBSL flux rope. Similar to Török, T. et al. (2010), Xu et al. (2020), and Guo et al. (2023), the theoretical curve path (r, θ, ϕ) is defined as below,

$$f = \begin{cases} \frac{s(2x_c - s)}{x_c^2} \theta_{ORIEN}, & \text{if } 0 \leq s \leq x_c \\ \frac{(s - 2x_c + 1)(1 - s)}{(1 - x_c)^2} \theta_{ORIEN}, & \text{if } x_c < s \leq 1 \end{cases},$$

$$\begin{cases} \phi = \phi_{BEG} + ((s - x_c)\cos f + x_c) LEN, & 0 \leq s \leq 1 \\ \theta = \theta_{BEG} + ((s - x_c)\sin f) LEN, & 0 \leq s \leq 1 \\ r = \begin{cases} R_s + \frac{x(2x_h - x)}{x_h^2} h, & \text{if } 0 \leq x \leq x_h \\ R_s + \frac{(x - 2x_h + 1)(1 - x)}{(1 - x_h)^2} h, & \text{if } x_h < x \leq 1 \end{cases} \end{cases} \quad . \quad (8)$$

The shape of the theoretical curve path is determined by parameters θ_{ORIEN}, x_c, x_h and h.

In this paper, we set $\theta_{ORIEN} = \frac{\pi}{6}$, $x_c = x_h = 0.5$, $LEN = \frac{\pi}{6}$, $h = 120\,\text{Mm}$, $a = 35\,\text{Mm}$, $F = 2 \times 10^{20}\,\text{Mx}$ and $I = -\frac{5\sqrt{2}F}{3\mu_0 a}$. The position of this RBSL flux rope in coronal region is determined by θ_{BEG} and ϕ_{BEG}, we set $\theta_{BEG} = \frac{\pi}{2}$ which is the same latitude of equator, and $\phi_{BEG} = \frac{235\pi}{180}$. In Fig. 1, we demonstrate the "S" shape axis path (a) and the magnetic field lines (b-d) of the RBSL flux rope. They are illustrated in a reference coordinate with an x axis determined by the intersection of the solar equator and the meridian plane, which crosses the midpoint of the line connected by the axis path's two-foot points, the z axis parallel to the polar axis of the Sun and the y axis defined by the right-hand rule. This theoretical axis path is symmetrical with respect to a plane parallel to the z axis, (a) the magnetic field lines are viewed from x (b) y (c) and z (d) directions, respectively, and the magnetic field strength of the flux rope reaches 13 Gauss near the footpoints of this "S" shape axis path.
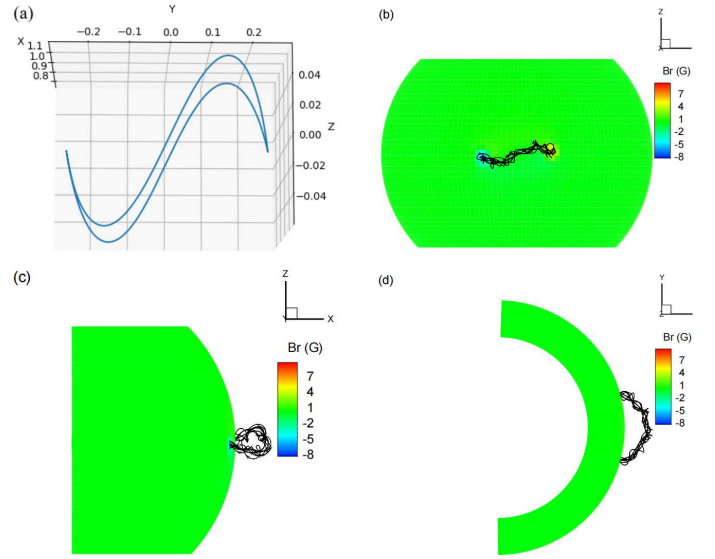
Fig. 1. Illustration of the theoretical "S"-shape axis path (a) and the magnetic field lines (b, c, d) of the flux rope. The x-axis is determined by the intersection of solar equator and the meridian plane which crosses the midpoint of the line connected by the axis path's two foot points, the z-axis coincides with the solar polar axis, and the y-axis is determined by the right-hand rule, and the units of these axes are R_s. The magnetic field lines in pictures b, c, and d are viewed from the directions of x, y, and z.

3. Numerical method formulation

In this section, we present the numerical method formulations used in this SIP-IFVM coronal model to reproduce the quasi-steady corona and to mimic the evolution and propagation process of CMEs. We briefly describe the discretization of the decomposed MHD equations, introduce the pseudo-time marching method, and demonstrate how the inner-boundary condition is implemented. In such formulation, a GSP-LSQ method coupled with a continuously differentiable weighted biased averaging procedure (WBAP) limiter (Feng 2020a; Li et al. 2011; Li & Ren 2012) is utilized to reconstruct the magnetic field, Godunov-Powell source terms are discretized in a way that can be incorporated to inviscid flux, the pseudo-time marching method is used to guarantee temporal accuracy of the implicit backward Euler solver with time-step size exceeding the CFL condition. Meanwhile, the "no-back flow" boundary condition (Feng et al. 2021; Groth et al. 2000; Wang et al. 2022a,b) is adopted to implement boundary conditions at the inner boundary.

3.1. Solver Description

In this paper, we adopt Godunov's method to advance cell-averaged solutions in time by solving a Riemann problem at each cell interface (Einfeldt et al. 1991; Godunov 1959). By integrating Eq. (2) over the hexahedral cell i and using Gauss's theorem to calculate the volume integral of the divergence of flux, we reach the following discretized equation

$$V_i \frac{\partial \mathbf{U}_i}{\partial t} = -\oint_{\partial V_i} \mathbf{F} \cdot \mathbf{n} d\Gamma + V_i \mathbf{S}_i, \quad (9)$$

where $\oint_{\partial V_i} \mathbf{F} \cdot \mathbf{n} d\Gamma = \sum_{j=1}^{6} \mathbf{F}_{ij} \cdot \mathbf{n}_{ij} \Gamma_{ij}$ and $\mathbf{S}_i = \mathbf{S}_{\text{Powell},i} + \mathbf{S}_{\text{gra},i} + \mathbf{S}_{\text{rot},i} + \mathbf{S}_{\text{heat},i}$. Hereafter $\mathbf{U}_i$ and $\mathbf{S}_i$ means the cell-averaged solution variable and source term in cell i, V_i is the volume of cell i, Γ_{ij} means the interface shared by cell i and its neighboring cell cell j, and also denote the area of this interface, $\mathbf{n}_{ij}$ is the unit normal vector of Γ_{ij} and points from cell i to cell j. As did in Feng et al. (2021) and Wang et al. (2022a), $\mathbf{S}_{\text{gra},i}$ and $\mathbf{S}_{\text{rot},i}$ are calculated by substituting the corresponding variables at the centroid of cell i into Eq. (3), $\mathbf{S}_{\text{Powell},i}$ is calculated by employing Gauss's law and mean value theorem. The inviscid flux through the interface Γ_{ij}, $\mathbf{F}_{ij} \cdot \mathbf{n}_{ij} = \mathbf{F}_{ij}(\mathbf{U}_L, \mathbf{U}_R) \cdot \mathbf{n}_{ij}$, is calculated by the positive-preserving HLL Riemann solver (Feng et al. 2021). Here and hereafter, the subscripts "$_L$" and "$_R$" denote the corresponding variables on Γ_{ij} extrapolated from cell i and cell j, respectively. Additionally, the cell-averaged heat source terms $\mathbf{S}_{\text{heat},i} = (0, \mathbf{S}_{m,i}, Q_{e,i} + \mathbf{v}_i \cdot \mathbf{S}_{m,i} + (\nabla \cdot \mathbf{q}), \mathbf{0})^T$ are calculated in a similar way as did in Wang et al. (2022a). It means that $\mathbf{S}_{m,i}$, $Q_{e,i}$, and $\mathbf{v}_i$ are defined as the corresponding variables at the centroid of cell i, and $(\nabla \cdot \mathbf{q})_i$ is calculated by Green-Gauss method, $(\nabla \cdot \mathbf{q})_i = \frac{1}{V_i} \sum_{j=1}^{6} \mathbf{q}_{ij} \cdot \mathbf{n}_{ij} \Gamma_{ij}$ where $\mathbf{q}_{ij}\left(T_L, T_R, (\nabla T)|_i, (\nabla T)|_j, \mathbf{U}_L, \mathbf{U}_R\right)$ is the heat flux through Γ_{ij}.

As we see, the state variables as well as derivatives of temperature on the cell surface Γ_{ij} are required in the calculation of inviscid flux and heat conduction term through Γ_{ij}. For convenience of calculation, we utilize a second-order positivity-preserving reconstruction method to calculate the piece-wise polynomial of a primitive variable.

$$X_i(\mathbf{x}) = X|_i + \Psi_i \, \nabla X|_i \cdot (\mathbf{x} - \mathbf{x}_i) \tag{10}$$

where $X \in \{\rho, u, v, w, p\}$, $X|_i$ is the corresponding variable at $\mathbf{x}_i$, the centroid of cell i, and $\nabla X|_i = \left(\frac{\partial X}{\partial x}, \frac{\partial X}{\partial y}, \frac{\partial X}{\partial z}\right)\Big|_i$ is the derivative of X at $\mathbf{x}_i$. Ψ_i is the limiter used to control spatial oscillation. Meanwhile, the temperature at the cell centroid is derived from equation of state $T|_i = \frac{p|_i}{\Re \rho|_i}$ and the reconstruction formulation of temperature in cell i, denoted by $T_i(\mathbf{x})$, is also calculated by Eq. (10). As usual, a shock detector (Feng et al. 2021; Li & Ren 2012) is used to determine whether a Barth-limiter (Barth & Jespersen 1989) should be triggered to control spatial oscillation for ρ, u, v, w, p, T.

For the magnetic field, a globally solenoidality-preserving (GSP) approach (Feng et al. 2019, 2021) is employed to maintain the divergence-free constraint, $\frac{1}{V_i} \sum_{j=1}^{6} \mathbf{B}_{ij} \cdot \mathbf{n}_{ij} \Gamma_{ij} = 0$, by performing an iteration procedure when reconstructing $\mathbf{B}_0$ and $\mathbf{B}_1$ on the cell interface. However, applying a limiter to the magnetic field can compromise its divergence-free constraint and may also increase discretization error in the magnetic field. Considering that $(\mathbf{B} + \epsilon \mathbf{B})^2 - \mathbf{B}^2 \equiv 2\epsilon \mathbf{B}^2 + \epsilon^2 \mathbf{B}^2$, the discretization error in magnetic pressure caused by the increased discretization error of magnetic field, denoted by $\epsilon \mathbf{B}$, can be comparable to thermal pressure and non-physical negative thermal pressure may appear when deriving thermal pressure from energy density, especially in low β regions. Therefore, in addition to utilizing decomposed MHD equations, we discard the limiter for the magnetic field during the quasi-steady coronal simulation to avoid degradation in precision and divergence-free constraint of the magnetic field. However, in the following time-varying CME simulations, a limiter for the magnetic field is still necessary to control spatial oscillation. In this paper, we adopt a continuously differentiable

WBAP limiter (Feng 2020a; Li et al. 2011; Li & Ren 2012) for $\mathbf{B}_1$ as described in Eq. 11 and constrain the max iteration for GSP to 5 as a prelim attempt, and we found it worked well in our CME simulations.

$$X_i(\mathbf{x}) = X|_i + \begin{pmatrix} \psi_{i,1}^{\text{WBAP}} \frac{\partial X}{\partial x} \\ \psi_{i,2}^{\text{WBAP}} \frac{\partial X}{\partial y} \\ \psi_{i,3}^{\text{WBAP}} \frac{\partial X}{\partial z} \end{pmatrix}\Bigg|_i \cdot (\mathbf{x} - \mathbf{x}_i)$$

with $\psi_{i,\xi}^{\text{WBAP}}(1, \vartheta_1, \vartheta_2, \cdots, \vartheta_6) = \tag{11}$

$$\begin{cases} \dfrac{n + \sum_{j=1}^{6} \frac{1}{\vartheta_{j,\xi}^{q-1} + \epsilon}}{n + \sum_{j=1}^{6} \frac{1}{\vartheta_{j,\xi}^{q} + \epsilon}}, & \text{if } \vartheta_1, \vartheta_2, \cdots, \vartheta_6 > 0 \\[2mm] 0, & \text{else} \end{cases},$$

where $\vartheta_{j,\xi} = \frac{\partial X}{\partial \xi}\big|_j / \frac{\partial X}{\partial \xi}\big|_i$ with $j \in \{1, 2, \cdots, 6\}$, $\xi \in \{x, y, z\}$ and $X \in \{B_{1x}, B_{1y}, B_{1z}\}$. ϵ, n and q are adjustable parameters and we set $\epsilon = 10^{-8}$, $n = 1$ and $q = 4$ in this paper.

3.2. Implementation of inner boundary condition

Figure 2 shows a 2D illustration of the inner-boundary cells, for example, cell -1, which lay on the leftmost layer of this picture. Gp1 and Gp2 are two Gaussian points on the inner-boundary face and points -1 and 0 are the cell centroids of cell -1 and cell 0 respectively. To update solutions on cell 0, we should calculate inviscid and heat flux through the surface of cell 0, including the interface shared by cell -1 and cell 0. It means we should calculate the reconstruction formulation of variables inside cell -1 and provide the values of these variables on the interface shared by cell -1 and cell 0 by this reconstruction formulation.
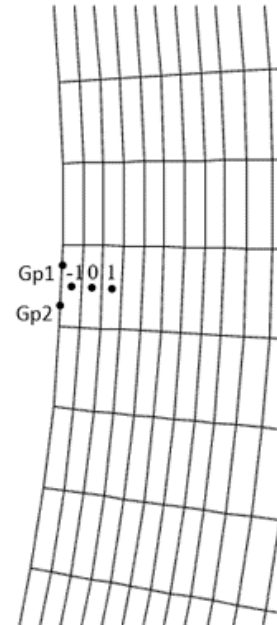
Fig. 2. 2D illustration of the inner boundary cells which lay on the leftmost layer of this picture.

In this paper, we use the Gaussian points (Gp1 and Gp2 in the 2D illustration) on the inner-boundary face, centroid point of the inner-boundary cell, cell -1 for example, and centroid

points of cell −1's five neighboring cells which share an interface with this hexahedral cell as the reconstruction stencil. Based on the former works (Feng et al. 2007, 2019, 2021; Groth et al. 2000; Wang et al. 2022a), we implement the condition of no "backflow" at these Gaussian points of the inner-boundary face for both quasi-steady coronal and time-dependent CME simulations. During these simulations, the inner boundary conditions are divided into two cases according to the flow with the radial speed of v_r in the cell adjacent to the inner boundary cell in the radial direction.

Case 1: If $v_r < 0$, then $\frac{\partial \rho}{\partial r} = 0$, $\frac{\partial p}{\partial r} = 0$, $\frac{\partial T}{\partial r} = 0$, $\mathbf{v} = 0$ and
$\mathbf{B} = \begin{cases} \mathbf{B}_0, & \text{for quasi-steady simulation} \\ \mathbf{B}_0 + \mathbf{B}_{FR}, & \text{for CME simulation} \end{cases}$,

Case 2: If $v_r \geq 0$, then $\rho = 1$, $p = \frac{1}{\gamma}$, $T = 1$, $\frac{\partial v_r}{\partial r} = 0$, $v_{t1} = 0$,
$v_{t2} = 0$ and $\mathbf{B} = \begin{cases} \mathbf{B}_0, & \text{for quasi-steady simulation} \\ \mathbf{B}_0 + \mathbf{B}_{FR}, & \text{for CME simulation} \end{cases}$, here v_{t1}
and v_{t2} are tangential velocities.

Similar to Feng et al. (2021) and Wang et al. (2022a), these boundary conditions are used to constrain the following reconstruction formulations.

$$X_{-1}(\mathbf{x}) = X|_{-1} + \psi_{-1} (\nabla X)|_{-1} \cdot (\mathbf{x} - \mathbf{x}_{-1}),$$
$$X \in \{\rho, u, v, w, \mathbf{B}_1, \mathbf{B}_0, p, T\}, \quad (12)$$

where $\mathbf{x}$ is a point inside cell −1, $\mathbf{x}_{-1}$ is the centroid position of cell −1, $X|_{-1}$ is the corresponding variable at $\mathbf{x}_{-1}$ and $X|_{-1}$ is constant during the simulation, and $(\nabla X)|_{-1} = \left(\frac{\partial X}{\partial x}, \frac{\partial X}{\partial y}, \frac{\partial X}{\partial z}\right)\Big|_{-1}$ denotes the derivative of X at $\mathbf{x}_{-1}$. In this paper, $(\nabla X)|_{-1}$ is obtained by solving a least-square problem (Barth 1991, 1993), and ψ_{-1} is defined as a Barth-limiter (Barth & Jespersen 1989).

3.3. Pseudo-time marching method

In this paper, we perform a backward Euler temporal integration on Eq. (2) and reach the following equation,

$$V_i \frac{\Delta \mathbf{U}_i^n}{\Delta t} + \mathbf{R}_i^{n+1} = \mathbf{0}. \quad (13)$$

The superscripts "n" and "$n+1$" denote the time level, $\mathbf{R}_i^{n+1} = \sum_{j=1}^{6} \mathbf{T}_8^{-1} \mathbf{f}_{ij} \left(\mathbf{U}_{nL}^{n+1}, \mathbf{U}_{nR}^{n+1}\right) \Gamma_{ij} - V_i \mathbf{S}_i^{n+1}$ means the residual operator over cell i at the $(n+1)$-th time level, $\Delta \mathbf{U}_i^n = \mathbf{U}_i^{n+1} - \mathbf{U}_i^n$ is the solution increment between the n-th and $(n+1)$-th time level, and Δt is the time increment. Referring to Wang et al. (2022a) and Xia et al. (2018), we have

$$\Delta t = \min (\Delta t_d, \Delta t_c), \quad \Delta t_c = \text{CFL} \cdot \min_{\forall \text{cell } i} \frac{\Delta h_i}{\max_{\forall \text{faces}} (|v_n| + c_f)},$$
$$\Delta t_d = \text{CFL} \cdot \min_{\forall \text{cell } i} \frac{\Delta h_i^2}{(\gamma - 1) \xi \max_{\forall \text{faces}} c_{An}^2} \quad (14)$$

where Δh_i is defined as the diameter of the inscribed sphere in cell i, v_n, c_f and c_{An} are the normal plasma velocity, normal fast magnetosonic speed and normal Alfvén speed on cell i's surface respectively, and CFL is the Courant number. In the quasi-steady coronal simulations, CFL evolves from 0.5 and is increased by five at each time step until Δt reaches a predefined reference time length τ_{flow} which is the same as defined in Feng et al. (2021) and Wang et al. (2022a). In our simulations, the values of τ_{flow} are 0.112 and 0.057 hours, and the corresponding CFLs in Δt

formula denoted by Eq. (14) are around 100.5 and 250.5 for CR 2219 and the ad hoc case with initial magnetic field strength multiplied by 5, respectively.

As did in Wang et al. (2022a), an approximate local time linearization is performed for the residual operator $\mathbf{R}_i^{n+1}$ at $(t^n, \mathbf{U}_i)$ with respect to time as follows,

$$\mathbf{R}_i^{n+1} \approx \mathbf{R}_i^n + \left(\frac{\partial \mathbf{R}_i'}{\partial \mathbf{U}_i}\right)^n \Delta \mathbf{U}_i^n + \sum_{j=1}^{6} \left(\frac{\partial \mathbf{R}_i'}{\partial \mathbf{U}_j}\right)^n \Delta \mathbf{U}_j^n$$

where $\Delta \mathbf{U}_{i/j}^n = \mathbf{U}_{i/j}^{n+1} - \mathbf{U}_{i/j}^n$ is the solution increment in cell i and cell i's j-th neighboring cell, and $\mathbf{R}_i' = \sum_{j=1}^{6} \mathbf{T}_8^{-1} \mathbf{f}_{ij}' (\mathbf{U}_{nL}, \mathbf{U}_{nR}) \Gamma_{ij} - V_i \mathbf{S}_i$. The same to Wang et al. (2022a), the modified numerical flux $\mathbf{f}_{ij}' (\mathbf{U}_{nL}, \mathbf{U}_{nR})$ is calculated by adding an appropriate viscous term to $\mathbf{f}_{ij} (\mathbf{U}_{nL}, \mathbf{U}_{nR})$ (Otero & Eliasson 2015b,a) to help maintain a diagonally dominant Jacobian matrix with a smaller condition number. Consequently, Eq. (13) is approximated to a linearized system in form of Eq. (15),

$$\mathbf{A}'_{8N \times 8N} (\Delta \mathbf{U}^n)_{8N} = - (\mathbf{R}^n)_{8N} \quad (15)$$

where $\mathbf{A}'_{8N \times 8N} = \left(\frac{V}{\Delta t} \mathbf{I} + \left(\frac{\partial \mathbf{R}'}{\partial \mathbf{U}}\right)^n\right)_{8N \times 8N}$ is an approximate Jacobian matrix with N denoting the number of cells in computational domain, $(\Delta \mathbf{U}^n)_{8N} = \left(\mathbf{U}^{n+1}\right)_{8N} - (\mathbf{U}^n)_{8N}$ and $(\mathbf{R}^n)_{8N}$ denote the solution increment and residual operator on these N cells at the n-th time step, and $\left(\mathbf{U}^{n+1}\right)_{8N}$ and $(\mathbf{U}^n)_{8N}$ denote the conservative solutions on these N cells at the $n+1$-th and n-th time steps respectively. We solve Eq. (15) by the parallel implicit LU-SGS method (Feng et al. 2021; Wang et al. 2022a) which includes a forward sweep and a backward sweep with a higher order infinitesimal term neglected, and set $\left(\mathbf{U}^{n+1}\right)_{8N} = (\mathbf{U}^n)_{8N} + (\Delta \mathbf{U}^n)_{8N}$. We also carry out an identification for the quasi-steady state coronal condition (Wang et al. 2022a). We assign $\left(\mathbf{U}^{n+1}\right)_{8N}$ to the steady-state coronal solution as well as terminate the program once the quasi-steady-state coronal simulation is determined to have reached the steady-state condition on the n-th time step. To judge the steady-state condition promptly as well as avoid mistaking the unsteady-state as steady-state condition, we only trigger the identification of steady coronal condition when $t > \kappa \frac{R}{V_A}$ where $V_A = \frac{B_{s-ave}}{\sqrt{\rho_s}}$ with B_{s-ave} denoting the average magnetic field intensity on the solar surface, R being radius of the spherical computational domain, and κ denoting an adjustable parameter and we set $\kappa = 4$.

Once the quasi-steady coronal simulations are judged to reach a steady-state coronal structure, we insert the magnetic field of the RBSL flux rope into the background corona and then perform the time-dependent CME simulations. To improve the temporal accuracy for CME simulations, we further introduce a pseudo time τ to Eq. (13) and update the solution during each physical time step Δt by solving a steady-state problem on τ. Consequently, we achieve the following equation

$$V_i \frac{\Delta \mathbf{U}_i}{\Delta \tau} + \left(V_i \frac{\Delta \mathbf{U}_i^n}{\Delta t} + \mathbf{R}_i^{n+1}\right) = \mathbf{0}. \quad (16)$$

Here $\Delta \tau$ is a pseudo time step and $\Delta \mathbf{U}_i$ is the solution increment during $\Delta \tau$.

In this paper, we solve Eq. (16) by using backward Euler method as bellow,

$$V_i \frac{\mathbf{U}_i^{n,m+1} - \mathbf{U}_i^{n,m}}{\Delta \tau} = \left(V_i \frac{\mathbf{U}_i^n - \mathbf{U}_i^{n,m+1}}{\Delta t} - \mathbf{R}_i^{n,m+1}\right). \quad (17)$$

In Eq. (17), $\mathbf{U}_i^{n,m+1}$ and $\mathbf{U}_i^{n,m}$ denote the solution variables on $\tau^{n,m+1}$ and $\tau^{n,m}$, and $\mathbf{U}_i^{n,0} = \mathbf{U}_i^n$. Here and hereafter, the superscripts "n,m" and "$n,m+1$" denote the corresponding variable on the m-th and $(m+1)$-th pseudo time level during the n-th physical time step. Also, we implement an approximate local time linearization for the residual operator $\mathbf{R}_i^{n,m+1}$ at $(\tau^{n,m}, \mathbf{U}_i)$ with respect to pseudo time as below,

$$\mathbf{R}_i^{n,m+1} \approx \mathbf{R}_i^{n,m} + \left(\frac{\partial \mathbf{R}_i'}{\partial \mathbf{U}_i}\right)^{n,m} \Delta \mathbf{U}_i^{n,m} + \sum_{j=1}^{6} \left(\frac{\partial \mathbf{R}_i'}{\partial \mathbf{U}_j}\right)^{n,m} \Delta \mathbf{U}_j^{n,m}$$

where $\Delta \mathbf{U}_{i/j}^{n,m} = \mathbf{U}_{i/j}^{n,m+1} - \mathbf{U}_{i/j}^{n,m}$ is the solution increment at the m-th pseudo time step of the n-th physical time step in cell i and cell i's j-th neighboring cell. Consequently, Eq. (17) can be written as

$$\frac{V_i}{\Delta \tau}\left(\mathbf{U}_i^{n,m+1} - \mathbf{U}_i^{n,m}\right) = \frac{V_i}{\Delta t}\left(\mathbf{U}_i^n - \mathbf{U}_i^{n,m+1}\right) - \mathbf{R}_i^{n,m} - \left(\frac{\partial \mathbf{R}_i'}{\partial \mathbf{U}}\right)^{n,m}\left(\mathbf{U}^{n,m+1} - \mathbf{U}^{n,m}\right).$$

It means

$$\left(\frac{V_i}{\Delta \tau}\mathbf{I} + \frac{V_i}{\Delta t}\mathbf{I} + \left(\frac{\partial \mathbf{R}_i'}{\partial \mathbf{U}_i}\right)^{n,m}\right)\left(\mathbf{U}_i^{n,m+1} - \mathbf{U}_i^{n,m}\right) = \qquad (18)$$

$$\frac{V_i}{\Delta t}\left(\mathbf{U}_i^n - \mathbf{U}_i^{n,m}\right) - \mathbf{R}_i^{n,m} - \left(\frac{\partial \mathbf{R}_i'}{\partial \mathbf{U}_j}\right)^{n,m}\left(\mathbf{U}_j^{n,m+1} - \mathbf{U}_j^{n,m}\right).$$

As a result, we reach the following linearized system

$$\mathbf{A}_{8N \times 8N}''(\Delta \mathbf{U}^{n,m})_{8N} = \mathbf{b}_{8N} \qquad (19)$$

where $\mathbf{A}_{8N \times 8N}'' = \left(\frac{V}{\Delta \tau} + \frac{V}{\Delta t} + \left(\frac{\partial \mathbf{R}'}{\partial \mathbf{U}}\right)^{n,m}\right)_{8N \times 8N}$, $(\Delta \mathbf{U}^{n,m})_{8N} = \left(\mathbf{U}^{n,m+1}\right)_{8N} - (\mathbf{U}^{n,m})_{8N}$ and $\mathbf{b}_{8N} = \frac{V}{\Delta t}((\mathbf{U}^n)_{8N} - (\mathbf{U}^{n,m})_{8N}) - (\mathbf{R}^{n,m})_{8N}$.

In this paper, we solve Eq. (19) by the parallel implicit LU-SGS method (Feng et al. 2021; Wang et al. 2022a). In Eq. (19), Δt is formulated by Eq. (14), and CFL evolves from 0.5 and is added by five at each physical time step until Δt reaches $\chi \cdot \tau_{flow}$ where χ is an adjustable parameter. Afterward, $\Delta t = \chi \cdot \tau_{flow}$ advances solutions on the following physical time steps. The time-step size Δt can affect the solution accuracy and computational efficiency for time-dependent simulations. Selecting a considerable time step in the implicit method usually leads to a loss in temporal accuracy. In contrast, a small time step leads to more time steps and requires more computing resources. To find a suitable time step that can both maintain a required temporal accuracy and a desired high computational efficiency, we set $\chi = 1$, 0.5, 0.25, 0.125 respectively, and compare the effects of different Δt on simulation results in Section 4.

Also, the pseudo-time-step size $\Delta \tau$ can affect the convergence rate of the steady-state simulation in pseudo-time τ. We set $\Delta \tau = 10^{20}$ in the initial pseudo time step of the n-th physical time step and get $\left(\mathbf{U}^{n,1}\right)_{8N} = \left(\mathbf{U}^{n,0}\right)_{8N} + \left(\Delta \mathbf{U}^{n,0}\right)_{8N}$. By this mean $\left(\mathbf{U}^{n,1}\right)_{8N}$ serves as a good preliminary guess for the steady-state solution on τ. In the following pseudo time steps during the n-th physical time step, we set $\Delta \tau = \Delta t$ to gradually evolve the solution from $\left(\mathbf{U}^{n,1}\right)_{8N}$ to the steady state solution on τ of the n-th physical time step. This strategy helps to guarantee both numerical stability and computational efficiency. Meanwhile, the simulation is judged to reach the steady state condition on τ of the

n-th physical time step when $\frac{|(\Delta \mathbf{U}^{n,m})_{8N}|}{N} < \epsilon_1$ or $\frac{|(\Delta \mathbf{U}^{n,m})_{8N}|}{|(\Delta \mathbf{U}^{n,0})_{8N}|} < \epsilon_2$. Here ϵ_1 and ϵ_2 are two adjustable small parameters and we set $\epsilon_1 = 10^{-5}$ and $\epsilon_2 = \frac{1}{500}$ in this paper. Eventually, we set $\left(\mathbf{U}^{n+1}\right)_{8N} = \left(\mathbf{U}^{n,m+1}\right)_{8N}$ and stop the pseudo-time simulation of the n-th physical time step when the steady-state condition is satisfied at the m-th pseudo-time step of the n-th physical time step. For better computational efficiency, we limit the number of pseudo-time steps during a physical time step to be no more than N_τ and set $\left(\mathbf{U}^{n+1}\right)_{8N} = \left(\mathbf{U}^{n,N_\tau}\right)_{8N}$ once the number of pseudo-time steps during a physical time step reaches N_τ. In this paper, we set $N_\tau = 5$.

Considering that the forward-backwards sweep of an LU-SGS iteration can only update solutions of inner cells of a processor, but not solutions of ghost cells, and the solution information in ghost cells is also required in parallel LU-SGS method (Feng et al. 2021), we need carefully perform synchronized MPI data communication between different processors in the parallel LU-SGS method (Otero & Eliasson 2015a; Petrov et al. 2017; Sharov et al. 2000) to avoid degradation of the convergence rate. Interested readers can refer to Appendix B to see how we implement the data communication in our six-component composite grid system.

4. Numerical results

In this section, the SIP-IFVM coronal model developed in previous sections is first employed to mimic the quasi-steady state solar corona of Carrington rotations (CR) 2219 and then used to investigate the CME evolution and propagation procedure in the background solar corona. CR 2219 is around the solar minimum of the solar cycle (SC) 24 and persists from June 29, 2019, to July 26, 2019. As mentioned in Subsection 2.2, the initial magnetic fields for the quasi-steady state coronal simulation are achieved from the potential field (PF) model whose bottom boundary condition is specified by the synoptic maps of the radial photospheric magnetic field centered on 2019 July 2, which can be downloaded at https://gong.nso.edu/adapt/maps/gong/. Followed by the quasi-steady state solar coronal simulation, an RBSL flux rope with a theoretical-based "S"-shaped axis path is inserted into the steady corona to trigger the CME event. We compare the CME simulation results adopted at different considerable time-step sizes (CFL ≫ 1) with those achieved at small time-step sizes (CFL = 1) to validate the model's capability of accurately and efficiently calculating time-varying simulation with a relatively large time step. Furthermore, to demonstrate the implicit MHD model's capability of dealing with low plasma β problems, we perform an ad hoc simulation by artificially enhancing the initial magnetic field of the quasi-steady state coronal simulation and CME simulation with a factor of 5 and 2.5 respectively, and keeping the other initial parameters unchanged. It leads to a low plasma β of about 5×10^{-4} and strong magnetic field strength of about 53 Gauss for the background corona, and the magnetic field strength of the flux rope reaches 34 Gauss near the footpoints of the flux rope's "S" shape axis path. Besides, we carry out an Orszag-Tang MHD vortex simulation in Appendix A to show that the novel pseudo-time-marching method and parallel LU-SGS method adopted in this paper is capable of simulating small-scale unsteady-state flows. In future research, we will develop high-order schemes and consider more physical mechanisms to make this efficient and robust MHD coronal model capable of performing high-fidelity and more realistic simulations.

In this paper, all the calculations are performed on the Tier-2 supercomputer infrastructure from the Flemish Supercomputer Center (Vlaams Supercomputer Centrum-VSC), the Flanders' most highly integrated high-performance research computing environment (`https://www.vscentrum.be/`). Both simulations are completed on 192 CPU cores. The quasi-steady state simulations calculated by the SIP-IFVM coronal model for CR 2219 and the ad hoc simulation reach the steady state after 776 and 1243 time iterations, and the wall-clock time durations are 0.12 and 0.18 hours, respectively. What's more, the wall-clock times are less than 0.7 hours for the time-dependent CME simulations of 6 hours of physical time when a considerable time step $\Delta t \geq 0.125 \cdot \tau_{flow}$ is adopted for both simulations. Here, τ_{flow} is the predefined reference time length mentioned in Subsection 3.3 and constrains the time-step sizes. However, in the CME simulations with a small time step in which CFL = 1 is adopted, the corresponding wall-clock times are 2.61 and 18.03 hours for CR 2219 and the ad hoc simulation, respectively. It demonstrates that this SIP-IFVM MHD coronal model is very efficient and numerically stable in the calculation of both steady-state background coronal structures and time-dependent CME events.

In the following of this section and Appendix A, we present the results of the quasi-steady coronal simulations of CR 2219, the ad hoc case with artificially enlarged magnetic field, the corresponding time-varying CME simulations and the small-scale Orszag-Tang MHD vortex simulations.

4.1. Quasi-steady state simulations for CR 2219

This subsection presents the steady-state simulation results for CR 2219 obtained from the SIP-IFVM coronal model. We compare the modeled results with the solar coronal observations and compare the simulation results calculated by this SIP-IFVM coronal model and the SIP-IFVM coronal model's explicit counterpart. We adopt the following explicit 2nd-order Runge-Kutta scheme (Abbreviated as ERK2 and described by Eq. (20)) in this explicit MHD model and call it SIP-EFVM coronal model.

$$\mathbf{U}^{(1)} = \mathbf{U}^n + \Delta t \mathbf{R}\left(\mathbf{U}^n\right)$$
$$\mathbf{U}^{n+1} = \frac{1}{2}\mathbf{U}^n + \frac{1}{2}\left(\mathbf{U}^{(1)} + \Delta t \mathbf{R}\left(\mathbf{U}^{(1)}\right)\right) \quad (20)$$

Here, the formula for calculating Δt in Eq. (20) is the same as in Eq. (13), and we set CFL = 0.5 for CR 2219.

In the quasi-steady state coronal simulation calculated by the explicit coronal model, the steady state condition is reached after 78767 time iterations with a time step of around 5.6×10^{-4} hours for CR 2219, and the wall-clock time is 8.25 hours. Besides, the average relative difference in proton number density $RD_{ave,\rho}$ and radial velocity RD_{ave,V_r} between the steady-state results simulated by SIP-IFVM and SIP-EFVM coronal models are only 3.05% and 3.43% for CR 2219. Here $RD_{ave,\rho} = \sum\limits_{i=1}^{N}\left|\rho_i^{\text{SIP-IFVM}} - \rho_i^{\text{SIP-EFVM}}\right|/\sum\limits_{i=1}^{N}\rho_i^{\text{SIP-EFVM}}$ and $RD_{ave,V_r} = \sum\limits_{i=1}^{N}\left|V_{r_i}^{\text{SIP-IFVM}} - V_{r_i}^{\text{SIP-EFVM}}\right|/\sum\limits_{i=1}^{N}V_{r_i}^{\text{SIP-EFVM}}$, the superscripts "SIP-IFVM" and "SIP-EFVM" denote the corresponding variable calculated by the SIP-IFVM and SIP-EFVM respectively, and N is the number of cells in the computational domain. It means that our SIP-IFVM coronal model gained a speedup of 68.7× for CR 2219 compared to the explicit coronal model, and the steady-state coronal structures simulated by the implicit and explicit models are consistent.

4.1.1. The open-field regions in the solar corona

Coronal holes (CHs) are dark regions in the images observed in extreme ultraviolet (EUV) and soft X-ray channels due to low plasma density in CHs caused by the magnetic field lines from CHs that are open to interplanetary space. CHs are the most prominent features in the solar corona because their distributions vary from different solar activity phases (Feng et al. 2015, 2017, 2019; Frazin et al. 2007; Hayes et al. 2001; Linker et al. 1999; Petrie et al. 2011). Three types of CHs can be identified in the EUV and soft X-ray images of the solar corona. Polar CHs are located at both solar poles and often stretch to low latitudes, sometimes across the solar equator. Isolated CHs, often seen near solar maxima, are detached from polar CHs and scatter at low and middle latitudes. Transient CHs are associated with solar eruptive events, such as coronal mass ejections, solar flares, and eruptive prominences.

The right panel in Fig. 3 illustrates synoptic maps of the observations from the Atmospheric Imaging Assembly (AIA) telescope on board the Solar Dynamics Observatory (Lemen et al. 2012), which are available at `https://sdo.gsfc.nasa.gov/data/synoptic/`, and the distributions of open- and closed-magnetic field regions achieved from the simulations (left) for CR 2219. The synoptic maps of observation are generated by concatenating a series of meridian strips taken from full-disk images in a time duration of a complete CR (Hamada et al. 2018). The synoptic maps of these observations and simulations reveal that the simulation roughly captures the polar and isolates coronal holes.

This simulation well reproduces the northern polar CH covering almost all longitudes except the patch between 30° and 120° with the latitudes of 60°N pole-ward. It also well captures the southern polar CH, almost spanning all longitudes for latitudes of 65°S pole-ward. In both simulation and observation results, the southern polar CHs between longitudes of 80° and 180° extend from 65°S to about 30°S and the northern polar CH extend towards the equator from $(\theta_{\text{lat}}, \phi_{\text{long}}) = (65°N, 265°)$ and reach an isolated CH centered at $(\theta_{\text{lat}}, \phi_{\text{long}}) = (15°N, 280°)$, where "$\theta_{\text{lat}}$" stands for heliographic latitude and "ϕ_{long}" Carrington longitude. Besides, the isolated CH centered at $(\theta_{\text{lat}}, \phi_{\text{long}}) = (-15°S, 325°)$ is also reproduced by the SIP-IFVM model. However, the CH extending from the south pole to the solar equator is larger in the simulation results than in the observation results. It may be due to the spacecraft of SDO nearly orbiting in the plane of the solar equator, thus resulting in the poor observation of polar CHs. The discrepancy between the modeled and observed results in polar regions may also be attributed to inaccurate observations for both polar photospheric magnetic fields, the utilization of periodic conditions in the longitudinal direction during the simulations, and the coronal evolution during this period. According to both past simulated and observational studies (Abramenko et al. 2010; Sun et al. 2011; Yang et al. 2011), stronger magnetic fields in polar regions tend to result in larger areas of polar coronal holes, fewer presences of low- and middle-latitudinal isolated coronal holes, and flatter coronal magnetic neutral lines. In addition, these differences in the solar corona can propagate outward and cause different manifestations in the heliosphere (Riley et al. 2012). Therefore, the uncertainty caused by periodically missing and high noise levels presented in the observations of solar polar fields is a critical factor that causes differences between the observations and the results of 3D solar wind MHD simulations.
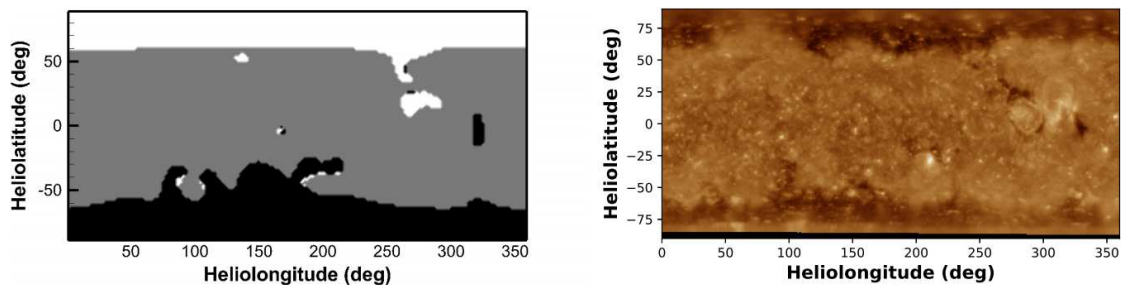
Fig. 3. Synoptic maps of the open-field regions modeled by the SIP-IFVM MHD model (left), and extreme ultraviolet observations from the 193 Å channel of AIA on board SDO (right) for CR 2219. In the synoptic map, the white and black patches denote open-field regions where the magnetic field lines point outward and inward to the Sun, respectively, and the grain patches denote the close-field region.

4.1.2. Simulated steady-state solar corona near the Sun

The white-light polarized brightness (pB) images can manifest the coronal structures seen in both limbs. In these pB images, bright regions represent coronal high-density structures, such as bipolar streamers and pseudo-streamers. In contrast, dark regions denote coronal low-density structures like coronal hole (Feng et al. 2015, 2017, 2019; Feng 2020b; Frazin et al. 2007; Hayes et al. 2001; Linker et al. 1999; Petrie et al. 2011). Bipolar streamers separate CHs of opposite magnetic polarities while pseudo-streamers separate CHs of the same polarity. Besides, bipolar streamers extend outward several solar radii from the Sun, and they are drawn into a cusp-like structure with a current sheet formed above the helmet streamer (Abbo et al. 2015; Feng et al. 2017, 2019; Riley et al. 2011; Wang et al. 2007).

In Fig. 4, we compare white-light pB images from 2.3 to $6R_s$ that observed from the Large Angle and Spectrometric Coronagraph C2 (Brueckner et al. 1995) on board the Solar and Heliospheric Observatory (SOHO), from 1.4 to $4R_s$ that observed by the innermost coronagraph of the Sun-Earth Connection Coronal and Heliospheric Investigation (SECCHI) instrument suite on board the Solar Terrestrial Relations Observatory Ahead (STEREO-A) spacecraft (Howard et al. 2008; Kaiser et al. 2008; Thompson et al. 2003; Thompson & Reginald 2008), both available at `https://stereo-ssc.nascom.nasa.gov/browse/` and synthesized from the results of the SIP-IFVM MHD coronal model (b, e). The observed and modeled images show a bright structure almost horizontally on the west limb in the LASCO-C2 view and the east limb in the STEREO-A view. In the LASCO-C2 and STEREO-A views, two narrow bright structures exist in the observed images, but only one is centered in the simulated result. However, the bright structures' center positions and widths are consistent in both observed and modeled images. From the close-ups of magnetic field lines ranging from 1 to $5R_s$ on the two selected meridian planes (c, f), we can deduce that the bipolar streamers produce bright structures. Furthermore, we make a comparison of the polarized brightness (pB) observations at 3 (left) and 5 (right) R_s and the modeled results in Fig. 5. In the figure, the bright structures represent distributions of the high-density coronal structures observed by SOHO/LASCO C2, and the black dashed and yellow solid lines denote the magnetic field lines (MNLs) modeled by the PFSS and the SIP-IFVM coronal models. It can be seen that the MNLs modeled by our SIP-IFVM coronal models are consistent with the MNLs from the PFSS model and the distributions of the high-density coronal structures observed by SOHO/LASCO C2.

In Fig. 6, we plot two-dimensional (2D) modeled magnetic field lines from 1 to $20R_s$ superimposed on contours of the radial

speed (left) and decadic logarithms of proton number density (right) on the meridian plane of $\phi_{\text{long}} = 250° - 70°$ for CR 2219. The figure indicates that the flows of high density and low speed (HDLS) are roughly centered around the latitude of $-8°$S in the half meridian plane of $\phi_{\text{long}} = 250°$ and 9°S in $\phi_{\text{long}} = 70°$, and the latitudinal width is about 30°. Meanwhile, the middle and high latitudes are dominated by the low-density and high-speed (LDHS) flow, which is a key characteristic of solar minima.

Furthermore, we demonstrate the distribution of relative difference of plasma density between the steady-state simulation results calculated by SIP-IFVM and SIP-EFVM coronal models in Fig. 7, with $\text{RD}_{\rho,i} = \left| \rho_i^{\text{SIP-IFVM}} - \rho_i^{\text{SIP-EFVM}} \right| / \rho_i^{\text{SIP-EFVM}}$. It can be seen that the relative difference decreases along the radial distance and is less than 5% in most regions. The average relative differences of plasma density, $\text{RD}_{\text{ave},\rho} = \frac{1}{N} \sum_{i=1}^{N} \text{RD}_{\rho,i}$ with N denoting the number of cells in the computational domain, calculated by SIP-IFVM and SIP-EFVM coronal model is 3.05%. Reminding that the SIP-IFVM coronal model is more than 60 times faster than the SIP-EFVM model in steady-state convergence rate, we can conclude that the SIP-IFVM coronal model can achieve results consistent with the explicit model with a significantly improved computational efficiency.

4.2. Time-dependent CME simulations

In this subsection, we insert the magnetic field of the RBSL flux rope with a theoretical "S"-shaped axis path described in Subsection 2.2 to the quasi-steady state solar corona of CR 2219 to trigger CME events. The pseudo-time marching method described in Subsection 3.3 mimics these CME evolution and propagation procedures from the solar surface to around 0.1 AU. First, we perform a CME simulation for CR 2219 with a small physical time step Δt. Then, we carry out four CME simulations with considerable physical time steps. Next, we compare the simulation results calculated by adopting different large Δt and those calculated by adopting small Δt. We set CFL = 1 in the simulation adopting small time step, and constrain $\Delta t \leq \chi \cdot \tau_{flow}$ as described in Subsection 3.3 and set $\chi = 1, 0.5, 0.25, 0.125$ respectively in these four CME simulations adopting large Δt.

As did in Linan et al. (2023) and Guo et al. (2023), we place a virtual satellite to monitor the variation pattern of solar coronal when disturbed by CMEs. In these CME simulations with large and small time steps, a virtual satellite was placed at point $(r, \theta, \phi) = (3R_s, 0°, 250°)$ to observe the changes of radial velocity V_r, plasma density ρ, thermal temperature T and plasma β. As illustrated in Fig. 8, there was a fluctuation of
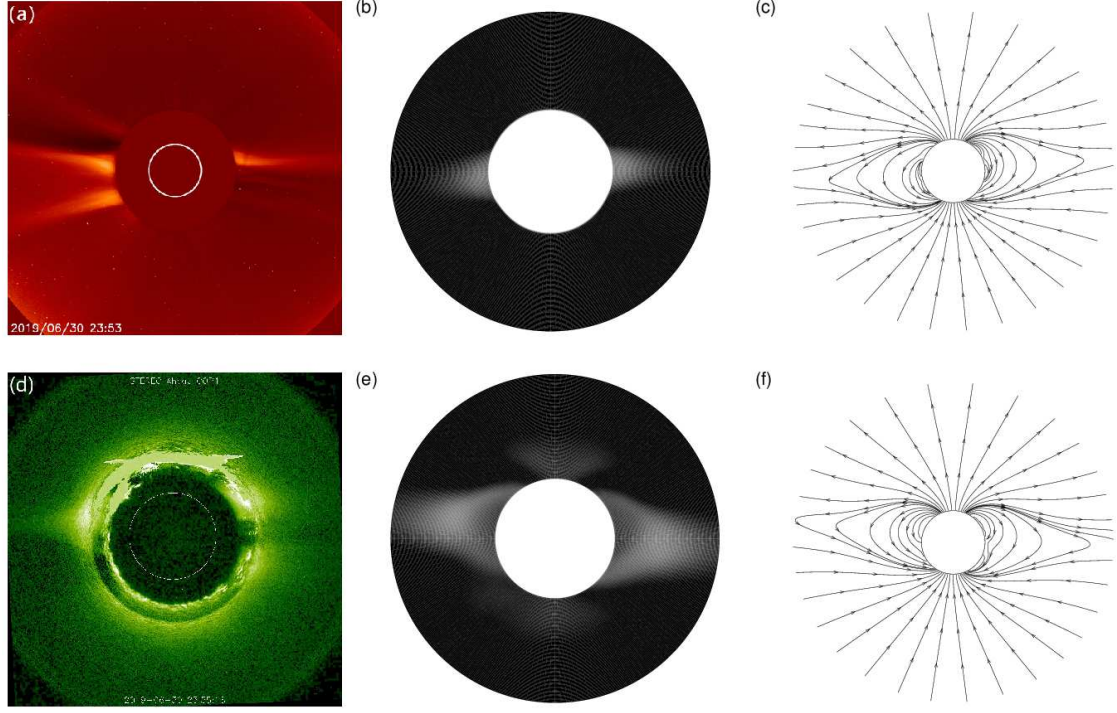
Fig. 4. White-light pB images observed from LASCO C2/SOHO (a) and COR1/STEREO-A (d) on June 30, 2019, corresponding pB images synthesized from simulation results (b, e), these synthesized images range from 2.3 to $6R_s$ on the meridian plane of $\phi_{\text{long}} = 250° − 70°$ (b) and range from 1.4 to $4R_s$ on the meridian plane of $\phi_{\text{long}} = 160° − 340°$ (e), respectively, and 2D simulated magnetic field lines from 1 to $5R_s$ on these two selected meridian planes (c, f).
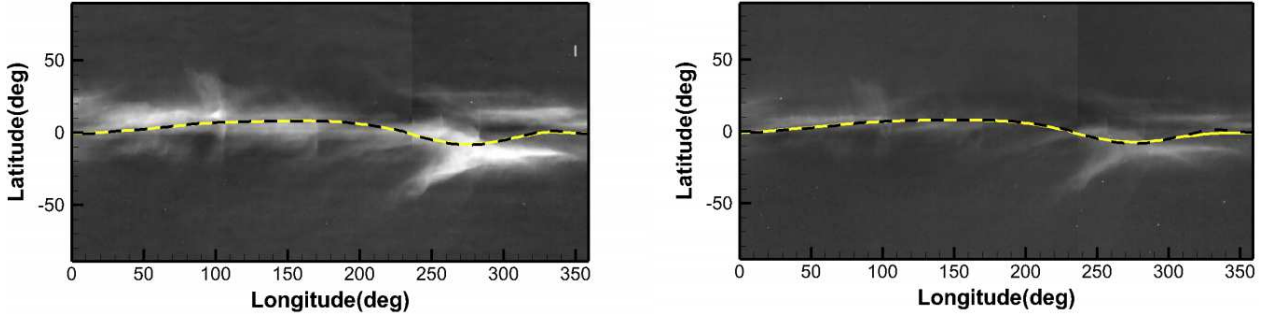

Fig. 5. Synoptic maps of white-light pB observations from SOHO/LASCO C2 at 3 (left) and 5 (right) R_s for CRs 2219. The yellow solid and black dashed lines denote the MNLs from the SIP-IFVM and the SIP-EFVM MHD coronal models, respectively.

V_r, ρ, T and β at about 0.6 hours of the CME simulations. Afterward, a peak appears in the profile of V_r, ρ, and T, and a trough appears at the profile of β. During the period of 0.6 and 1.0 hours of these CME simulations with different time-step sizes, the radial velocity all increased from 50 km s^{-1} to about 560 km s^{-1}, the number density increased from 2.3×10^5 cm^{-3} to 18×10^5 cm^{-3}, 14.8×10^5 cm^{-3}, 13.7×10^5 cm^{-3}, 13.2×10^5 cm^{-3} and 13.2×10^5 cm^{-3} for CFL = 1 and $\chi = 0.125$, 0.25, 0.5, 1, respectively. Though there was a delay in time for these parameters at large time steps compared to the results of small time steps, it is less than 0.1 hours for $\chi = 0.125$. Afterward, the radial velocity and number density decreased to 265 km s^{-1} and 4.9×10^5 cm^{-3}, respectively. During the period of 0.45 and 0.8 hours, the temperature increased from 16.35×10^5 K to 22.78×10^5 K and 22.84×10^5 K, then decreased to 14.4×10^5 K and 15.5×10^5 K at 1.12 and 1.25 hours, and then increased to 18.7×10^5 K and 18.5×10^5 K at 1.8 and 2.1 hours and decreased

to 17.6×10^5 K for CFL = 1 and $\chi = 0.125$, respectively. Though there are some differences in the value and arrival time of the peaks and troughs for the temperature profiles, the relative differences are still minimal for CFL = 1 and $\chi = 0.125$. As for the β, it decreased from about 18 to about one during the period of 0.45 and 0.65 hours, then increased to 8.3 and 4.7 at 0.85 hours and then decreased to 0.4 in the following time for CFL = 1 and $\chi = 0.125$, respectively. It shows that all of these CME simulations with large time steps, especially the large time steps with $\chi = 0.125$, exhibit consistent patterns of change with the simulation calculated by small time steps, and the CMEs modeled by different time-step sizes take almost the same physical time to arrive at this virtual satellite.

In Table 1, we further list the average relative differences in proton number density $\text{RD}^\chi_{\text{ave},\rho}$ and radial velocity $\text{RD}^\chi_{\text{ave},V_r}$ between the CME simulation results of large, $\Delta t = \chi \cdot \tau_{flow}$, and
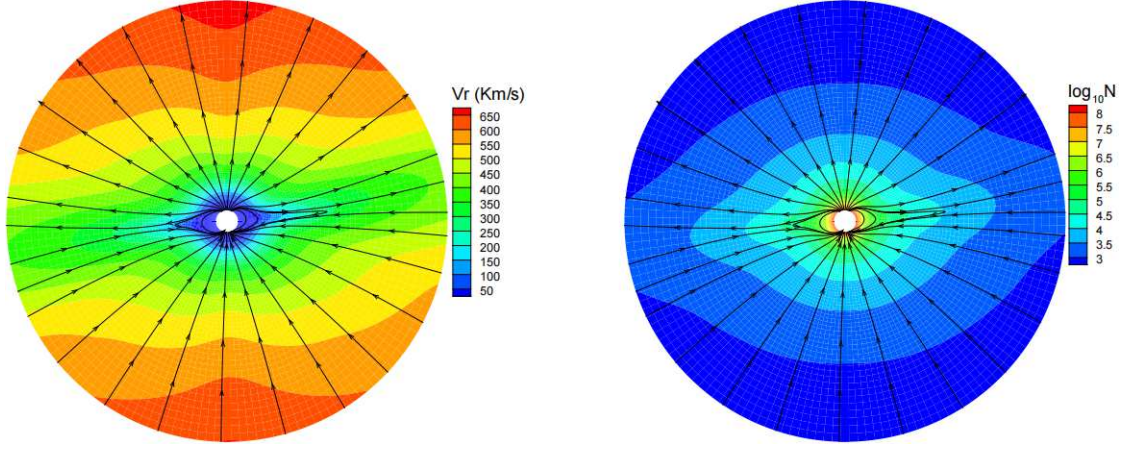
Fig. 6. Magnetic field lines from 1 to $20R_s$ overlaid on contours of the radial speeds $v_r \left(\text{km s}^{-1} \right)$ (left) and the decadic logarithms of the proton number density $N \left(\text{cm}^{-3} \right)$ (right) on the meridian planes of $\phi_{\text{long}} = 250° - 70°$ for CR 2219.
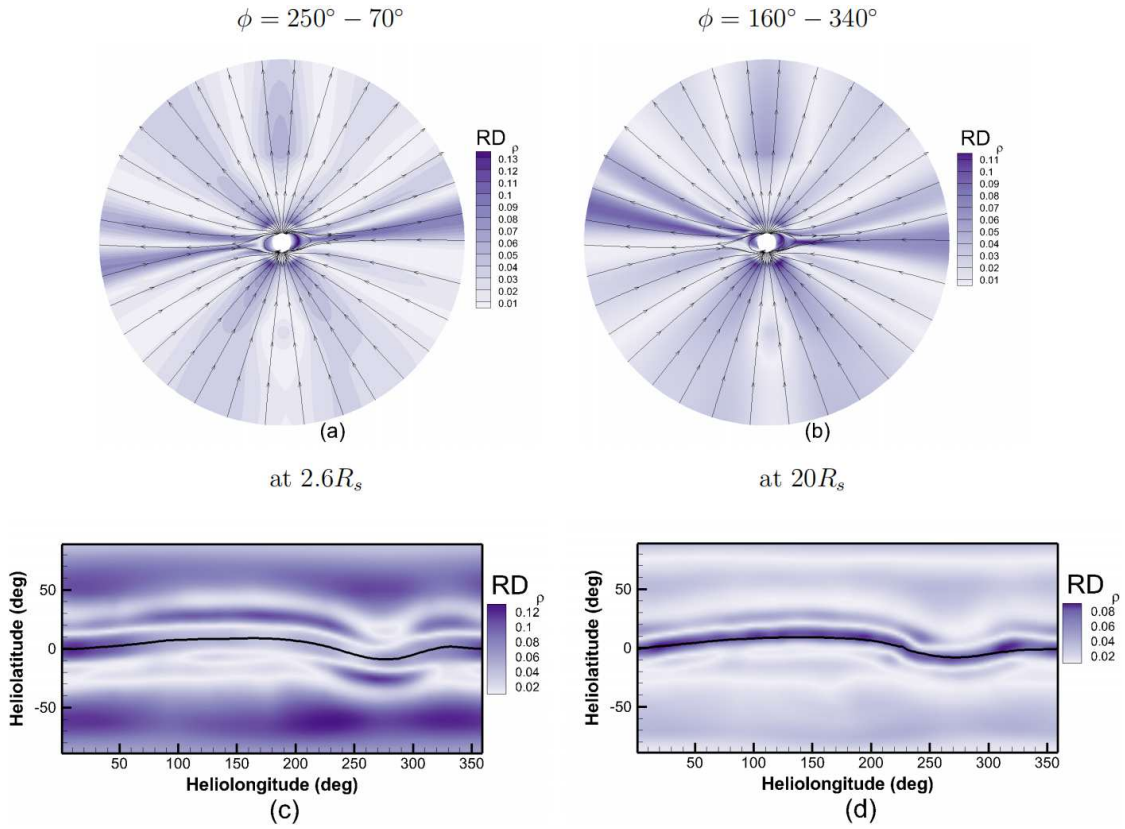
Fig. 7. Magnetic field lines from 1 to $20R_s$ overlaid on contours of the relative differences of plasma density on the meridian planes of $\phi_{\text{long}} = 250° - 70°$ (a) and $\phi_{\text{long}} = 160° - 340°$ (b) and synoptic maps for the relative differences of the plasma density at $2.6R_s$ (c) and $20R_s$ (d) for CR 2219. The white solid lines denote the MNLs from the SIP-IFVM MHD coronal model.

small, CFL = 1, physical time steps at different moments. Here $\text{RD}^{\chi}_{\text{ave},\rho} = \sum\limits_{i=1}^{N} \left| \rho_i^{\chi} - \rho_i^{\text{CFL}=1} \right| / \sum\limits_{i=1}^{N} \rho_i^{\text{CFL}=1}$ and $\text{RD}^{\chi}_{\text{ave},V_r} = \sum\limits_{i=1}^{N} \left| V_{r_i}^{\chi} - V_{r_i}^{\text{CFL}=1} \right| / \sum\limits_{i=1}^{N} V_{r_i}^{\text{CFL}=1}$. The superscripts "$\chi$" and "CFL=1" denote the corresponding variable calculated at large ($\Delta t = \chi \cdot \tau_{flow}$) and small (CFL = 1) physical time steps, respectively, and N is the number of cells in the computational domain.

It can be seen that the average relative differences of both density and radial velocity decrease with the decrease of physical time-step size. The relative differences of density and radial velocity are below 3% at different moments with $\chi \leq 0.5$. It means the relative differences of CME simulation results calculated at large and small time steps by this SIP-IFVM model can be no more than the relative differences between steady-state simulation results computed by SIP-IFVM and SIP-EFVM respectively but with obviously high computational efficiency. We are considering that the computational time of 6 hours of physical time is
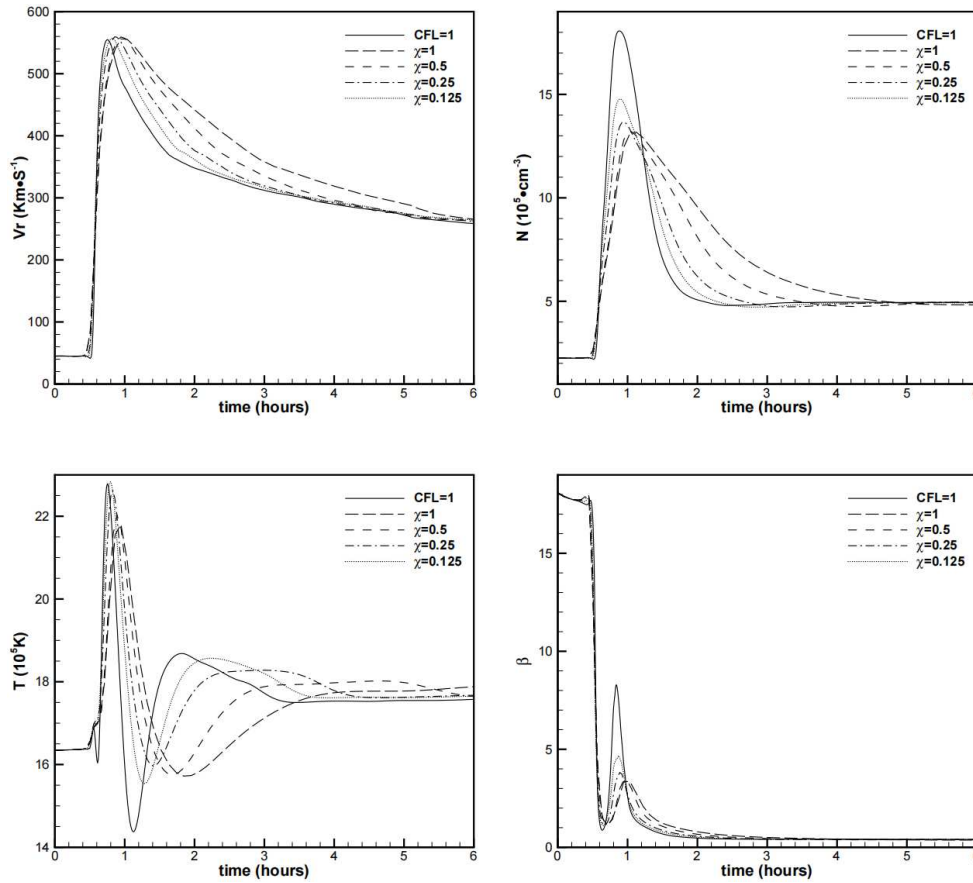
Fig. 8. In situ measurements of simulated radial velocity v_r $\left(\text{km s}^{-1}\right)$ (top left), proton number density $\left(10^5 \text{ cm}^{-3}\right)$ (top right), temperature $\left(10^5 \text{ K}\right)$ (bottom left) and plasma β (bottom right) by the virtual satellite placed at $(r, \theta, \phi) = (3R_s, 0°, 250°)$.

**Table 1.** Comparison of CME simulations for 6 hrs of physical time t.

Parameters	$\chi = 1$	$\chi = 0.5$	$\chi = 0.25$	$\chi = 0.125$
wall-clock time (hours)	0.08	0.14	0.26	0.43
$\text{RD}^{\chi}_{\text{ave},\rho}$ & $\text{RD}^{\chi}_{\text{ave},V_r}$ at t=1hr	2.19% & 1.54%	1.75% & 1.16%	1.17% & 0.72%	0.70% & 0.40%
$\text{RD}^{\chi}_{\text{ave},\rho}$ & $\text{RD}^{\chi}_{\text{ave},V_r}$ at t=3hrs	3.23% & 4.68%	2.24% & 2.86%	1.59% & 1.49%	1.14% & 0.71%
$\text{RD}^{\chi}_{\text{ave},\rho}$ & $\text{RD}^{\chi}_{\text{ave},V_r}$ at t=5hrs	3.52% & 4.29%	2.66% & 2.33%	2.09% & 1.18%	1.62% & 0.64%

only about 0.43 hours when $\chi = 0.125$, the computation efficiency can still be very high when adopting a smaller χ to get more accurate simulation results at the expense of an acceptable reduction in computation efficiency. We can adjust the physical time-step sizes according to the temporal accuracy required for our specific research or practical application work.

We demonstrate some CME simulation results calculated with $\chi = 0.125$ in the following.

In Fig. 9, we present snapshots of the magnetic field lines at 0, 1, 3, and 5 hours to demonstrate the propagation of the theoretical "S"-shaped flux rope in background coronal structures of CR 2219. These magnetic field lines are traced from the CME simulation results in a region of $(1R_s \leq r \leq 20R_s) \times (22.5° \leq \theta \leq 157.5°) \times (29° \leq \phi \leq 299°)$ and effectively capture the significant changes in the overall morphology of the CME flux rope as it propagates outward. The magnetic field lines are viewed in three orthogonal directions in the left, middle, and right panels. The left panels are viewed in the direction of

$(\theta, \phi) = (90°, 250°)$, and the sight directions are perpendicular to the meridian, which is parallel to the line connected by the flux rope's two footpoints. The middle panels are obtained by rotating the left panel 90° clockwise along the Z- axis, and the right panels are obtained by rotating the left panels 90° counterclockwise along the radial direction, which is parallel to the sight directions in the middle panels. It can be seen that the volume overlaid with the CME flux rope expands gradually, which may be attributed to the magnetic-pressure gradient between the flux rope and the surrounding solar atmosphere (Scolini, C. et al. 2019), and the magnetic reconnection occurring between the legs of the overlying field lines (Guo et al. 2023). Also, the topology of the magnetic field lines of the CME flux rope reveals a consistent evolution pattern with those simulated by the poly tropic MHD model (Guo et al. 2023), but with a faster-expanding velocity and more realistic thermodynamic evolution. Furthermore, we present snapshots of the radial speed V_r for CR 2219 at 1 (left), 3 (middle), and 5 (right) hours of the CME propagation
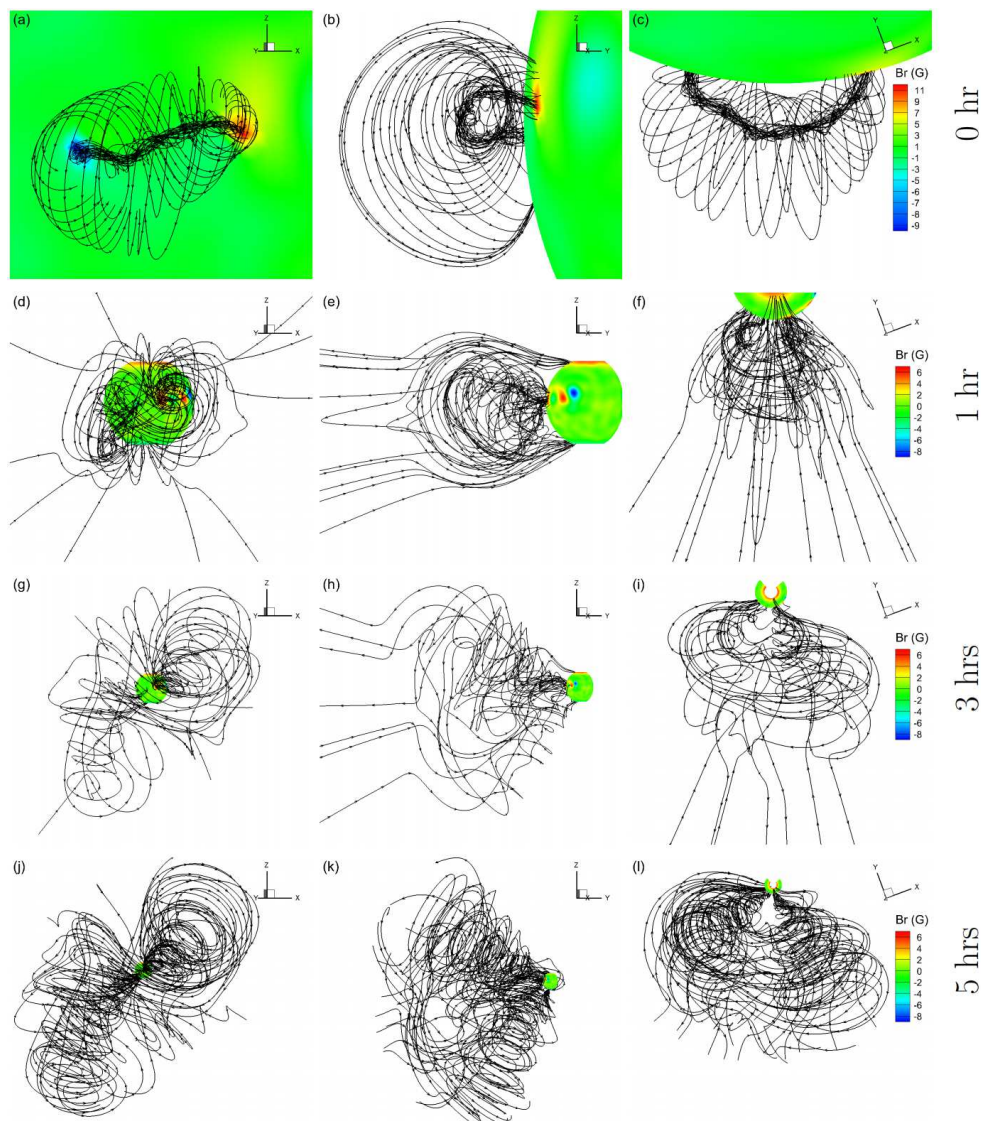
Fig. 9. 3D view of the magnetic field topology in the corona of CR 2219. These solid lines are representative magnetic field lines displaying the global evolution of the CME and traced from magnetic field in the region of $(1R_s \le r \le 20R_s) \times (22.5° \le \theta \le 157.5°) \times (29° \le \phi \le 299°)$ which encloses the theoretical "S" shape flux rope. The 1st, 2nd, 3rd and 4th panels correspond to the simulation results of the CME simulation at 0, 1, 3 and 5 hours, respectively. The magnetic field lines illustrated in left panel (a, d, g, j) are viewed from a direction of $(\theta, \phi) = (90°, 250°)$, the middle panel (b, e, h, k) from a direction of $(\theta, \phi) = (90°, 340°)$ and the right panel (c, f, i, l) from the direction of Z- axis, these three directions of sight are orthogonal to each other.

processes in Fig. 10. These 2D modeled contours of radial velocity are superimposed with magnetic field lines and range from 1 to $20R_s$ on the same meridian of Fig. 6. It can be seen that the exceptionally high speed appears at the regions where magnetic field lines change sharply, and the radial velocity can reach 900 km s^{-1}, which is consistent with the range of the speeds of observed CMEs (Chen 2011). It demonstrates that the model reproduces a CME with reasonable velocity and has the potential to produce a CME event consistent with observation. Using this model in our future research, we will make some observation-based CME simulations.

4.3. An ad hoc simulation with very low plasma β

In this subsection, we conduct a manufactured test by utilizing the SIP-IFVM model to mimic a very low-β problem. In the test simulation, we multiply the initial potential field of CR 2219

with a factor of 5 and then employ the SIP-IFVM model to achieve the quasi-steady state coronal structure. Fig. 11 displays the synoptic map of the magnetic field (left) and the corresponding plasma β (right) at a quasi-steady state near the solar surface. It can be seen that after enlarging the magnetic field strength, the local β value can be as small as 5×10^{-4}, and the magnetic field strength ranges from 5 to 50 Gauss in most regions near the solar surface. Moreover, it takes only 0.18 hours to converge to the steady state. In the CME simulation, we enhance the magnetic field of the flux roped described in Subsection 2.2 with a factor of 2.5, and set $\chi = 0.125$. It costs 0.67 hours to finish the time-dependent CME simulation of 6 hours of physical time. Compared with the simulation by small time steps (CFL=1), which cost 18.03 hours, this SIP-IFVM model is very efficient.

In Fig. 12, we illustrate the 2D magnetic field lines overlaid on contours of the radial speed (left) and decadic logarithms of the proton number density (right) on the selected plane for the
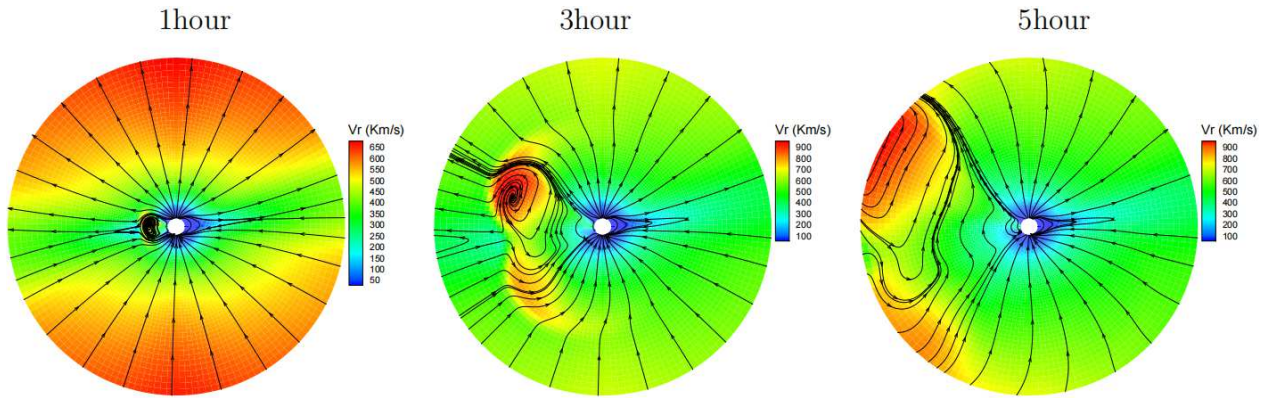
Fig. 10. Magnetic field lines from 1 to $20R_s$ overlaid on contours of the radial velocity on the meridian planes of $\phi_{\text{long}} = 250° - 70°$ for CR 2219. The left, middle, and right panels correspond to the simulation results at 1, 3, and 5 hours of the CME simulation, respectively.
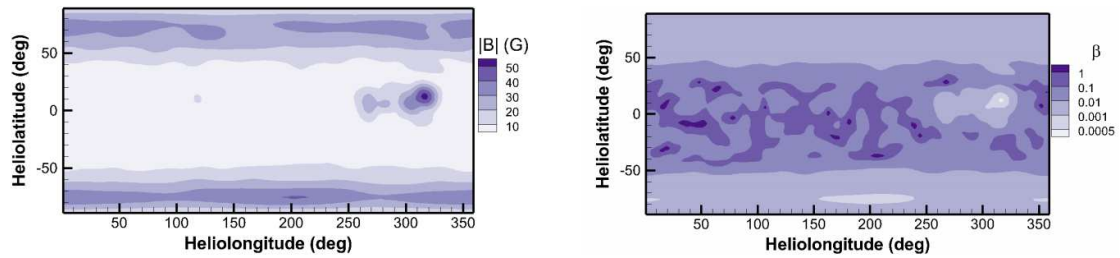
Fig. 11. Synoptic maps of the magnetic field strength in a unit of Gauss (left) and the plasma β distribution (right) at $1.015R_s$ for the test case with an enhanced magnetic field.

quasi-steady state result with an enlarged initial magnetic field. Comparing this with Fig. 6, it can be seen that the closed magnetic field lines near the Sun associated with coronal streamers extend farther to about $15\ R_s$, but their positions are almost the same. Moreover, the LDHS flow spans slightly larger latitudes for the I-MHD simulation with the enhanced initial magnetic field.

Also, we compare the simulation results calculated by large and small time steps. The average relative differences in proton number density and radial velocity between the CME simulation results of large ($\chi = 0.125$) and small (CFL = 1) physical time steps at 1, 2, and 3 hours are 3.91% and 1.69%, 6.10% and 3.08%, 6.43% and 4.08%, respectively. Furthermore, we adopt a smaller time step to check whether or not this SIP-IFVM model can get desirable accurate simulation results at the expense of an acceptable reduction in computation efficiency. We set $\chi = 0.025$ in this test case; the wall-clock time is 2.49 hours, and the corresponding average relative differences in proton number density and radial velocity at 1, 2, and 3 hours are only 1.33% and 0.75%, 1.98% and 1.74%, 2.08% and 2.33%, respectively. It demonstrates that the SIP-IFVM coronal model can still be accurate and efficient in mimicking complex problems with very strong magnetic fields.

In Fig. 13, we further present snapshots of the radial speed V_r and magnetic field lines at 1 (left), 2 (middle), and 3 (right) hours of the CME propagation processes for the manufactured test with enhanced magnetic fields. These 2D modeled contours of radial velocity are superimposed with magnetic field lines and illustrated on the same meridian of Fig. 10. It can be seen that a shock appears in this simulation, the volume overlaid with the flux rope magnetic field expands gradually. Though the topol-

ogy of magnetic field lines changes more gradually, the radial velocity of this shock is faster.

Furthermore, to check whether the novel pseudo-time-marching method and parallel LU-SGS method adopted in this paper are capable of simulating small-scale unsteady-state flows, we carry out an Orszag-Tang MHD vortex simulation in this Appendix A.

5. Conclusions

In this paper, we design an MHD model of the solar corona and CME with an efficient and time-accurate implicit strategy and call it the Solar Interplanetary Phenomena-Implicit Finite Volume Method (SIP-IFVM) coronal model. In this SIP-IFVM coronal model, the novel implicit strategy facilitates its numerical stability even at large time steps, which exceeds the CFL numerical stability limitation. This merit makes the SIP-IFVM coronal model capable of employing a large time step to accelerate the convergence rate in quasi-steady-state simulations and to reduce the calculation effort required in the time-dependent simulations. Also, the pseudo-time marching method which introduces a pseudo time τ at each physical time step and updates the solution of each physical time step by solving a steady-state problem on τ is used to improve the temporal accuracy of the implicit model at large time steps.

We utilize this model to reconstruct the steady-state coronal structure of CR 2219 and then introduce the magnetic field of an RBSL flux rope to the steady-state corona to trigger a CME event; afterward, we use the SIP-IFVM coronal model to simulate the CME propagation and evolution processes from the solar surface to $20\ R_s$ in the background corona of CR 2219. The modeled steady-state coronal structures are basically in agree-
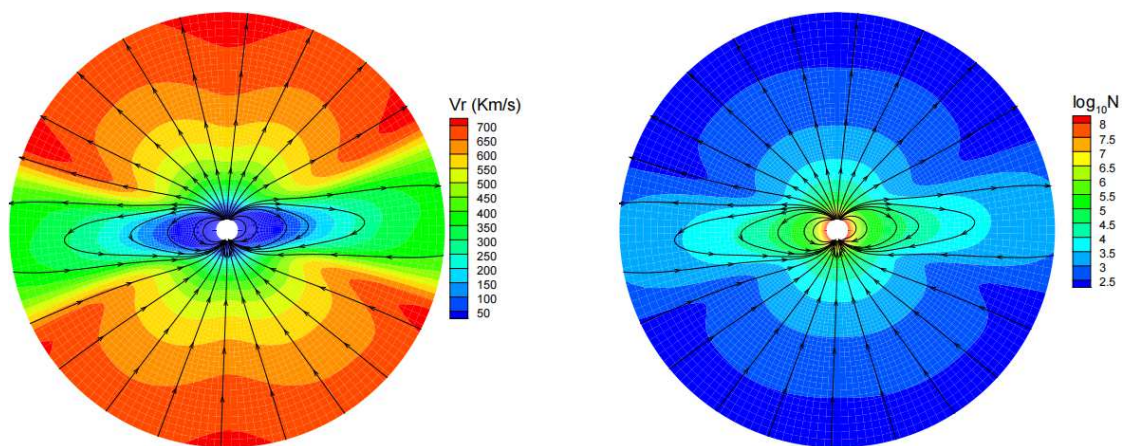
Fig. 12. Magnetic field lines from 1 to $20R_s$ overlaid on contours of the radial speeds v_r $\left(\text{km s}^{-1}\right)$ (left) and the decadic logarithms of the proton number density $N\left(\text{cm}^{-3}\right)$ (right) on the meridian planes of $\phi_{\text{long}} = 250° - 70°$ for the quasi-steady state result with enlarged initial magnetic field.
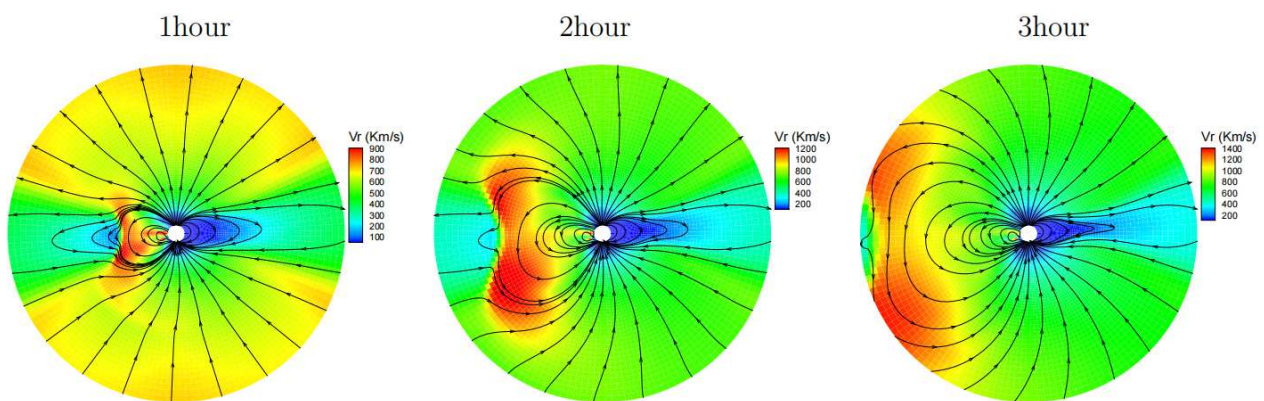
Fig. 13. Magnetic field lines from 1 to $20R_s$ overlaid on contours of the radial velocity on the meridian planes of $\phi_{\text{long}} = 250° - 70°$ for the manufactured test with enhanced magnetic fields. The left, middle, and right panels correspond to the simulation results at 1, 2, and 3 hours of the CME simulation, respectively.

ment with the remote sensing observations from SDO, SOHO, and STEREO-A, and the simulated CMEs present a reasonable evolution pattern of magnetic and flow fields. Furthermore, we conduct an ad hoc simulation by artificially enlarging the initial magnetic field of the background corona of CR 2219 and the RBSL flux rope; it demonstrates that the SIP-IFVM coronal model can robustly and efficiently deal with the time-dependent problems with plasma β as low as about 5×10^{-4}. Additionally, we perform an Orszag-Tang MHD vortex flow simulation, which shows that the pseudo-time-marching method adopted in this model is capable of simulating small-scale unsteady-state flows.

We can conclude that the SIP-IFVM coronal model has the following merits, providing strong justification for using a fully implicit scheme in time-dependent coronal and CME simulations.

1. The SIP-IFVM coronal model is both time-accurate and highly computationally efficient. Adopting large time steps can still yield consistent results, as those calculated at small time steps.
   Compared to the simulation using a small time-step size determined by the CFL stability restriction, by adopting an appropriate large time-step size, it achieves a speedup of over 6 × in CME simulations covering 6 hours of physical

time, with the average relative difference in plasma density, $\text{RD}_{\text{ave},\rho}$, being no more than 2.0%. Besides, by adopting a large time-step size, the implicit quasi-steady-state coronal model achieves a speedup of over 60 ×, with $\text{RD}_{\text{ave},\rho}$ being only 3.05%, compared to the explicit model. The total wall-clock time of the quasi-steady coronal and time-dependent CME simulations is less than 0.6 hours (192 CPU cores, ~ 1 M cells).

2. The SIP-IFVM coronal model can robustly and efficiently deal with time-dependent problems with extremely low plasma β regions.
   Compared to the simulation using a small time-step size determined by the CFL stability restriction, by adopting an appropriate large time-step size, it achieves a speedup of over 7 × in the ad hoc simulations where the plasma β can be as low as about 5×10^{-4}, with $\text{RD}_{\text{ave},\rho}$ being no more than 2.4%.

3. The SIP-IFVM coronal model can reproduce both a quasi-steady state coronal structure consistent with observations and an explosive CME event appearing with a reasonable evolution pattern of magnetic and flow fields.
   The relatively realistic simulation result and high flexibility in the practical implementation of CME simulations are guaranteed by adopting the thermodynamic MHD equations, which also consider the heat conduction term to account for energy exchanges, and utilizing the novel RBSL flux rope,

which can both trigger a CME event by only introducing the flux-rope magnetic field to the background corona and allow an arbitrary shape of the electric current path.

All these simulation results demonstrate that the SIP-IFVM model is very efficient and numerically stable and is promising to timely and accurately simulate time-varying events in solar corona with low plasma β in practical applications. In addition, we have also made some preliminary attempts to use the SIP-IFVM coronal model and observation-based RBSL flux rope to mimic a realistic CME event, and the CME simulation results are consistent with the white-light pB images observed from COR1/STEREO-A/B and COR2/STEREO-A/B. We will continue making observation-based CME simulations using this model and present these research works in future papers.

Although this established solar coronal is merited in many aspects and acts as a promising tool for reproducing the large-scale structures of the solar corona and timely and accurately simulating time-varying CME events in the solar corona, there is still room for further improvement. A proper modification of the Jacobian matrix in Eq. (15), which reduces the mismatch between the residual and Jacobian matrix, may lead to a better convergence rate (e.g. Otero & Eliasson 2015b; Xia et al. 2014). Further research on the calibration of the coronal and CME model based on remote sensing and in situ observation is still worthwhile to make the SIP-IFVM model perform better in reproducing more realistic results. Extending the SIP-IFVM coronal model to a high-order accurate model may make it capable of performing high-fidelity simulations to capture subtle structures during the time-dependent coronal simulations. In addition, it may be worthwhile to try starting the global coronal simulation from some more consistent low coronal simulation results. For example, try to use the initial magnetic field above an active region calculated by the low coronal magnetic-friction (MF) model and the evolving electric field at the photosphere derived from a time series of observed photosphere magnetic field to drive detailed MHD simulations of active regions (Hoeksema et al. 2020) in the SIP-IFVM global coronal model.

There are also some issues that are worth further discussion, and we will attempt to address these in our future research to further improve this model.

1. The pseudo-time iteration during each physical time can reduce computation efficiency. However, an appropriate physical time step size can help maintain required temporal accuracy without much reduction in computational efficiency, and a proper pseudo-time step can also help accelerate the steady-state simulation's convergence rate in pseudo-time τ. Although the physical-time steps and pseudo-time steps used in this paper perform well, more effective and flexible time-step adaptation strategies may be possible. We will try to find a better plan for selecting time-step sizes in our future research works.

2. Typically, the polytropic index γ is set to be larger than 1.05 to ensure numerical stability and physical realism in the simulation when a thermal conductivity term is considered. However, we discovered that maintaining $\gamma = 1.05$ still yields satisfactory results in our solar coronal simulations, even with the thermal conductivity term considered. Moreover, the inclusion of the thermal conductivity term helps to maintain energy balance, even when γ is set to 1.05. Consequently, we opted not to modify γ in this paper. Actually, the thermodynamic processes of the solar corona are highly intricate and susceptible to a variety of factors in MHD simulation. For example, different treatments of radiative losses,

anisotropic thermal conduction, coronal heating and even numerical diffusion may lead to some variations in the results of thermodynamic MHD coronal simulations. In the future, we will try to recover a uniform value of $\gamma = \frac{5}{3}$ after considering more thermodynamic mechanisms, such as the radiative losses and more consistent physical-based heating source terms.

Appendix A: Orszag-Tang MHD vortex problem

The Orszag-Tang vortex system includes many significant characteristics of MHD turbulence, and some shocks and other discontinuities occur in this MHD vortex flow as time evolves. It was first proposed by Orszag & Tang (1979), and is frequently used to test 2D MHD codes (Jiang & Wu 1999; Tóth 2000; Zhang et al. 2006; Zhou & Feng 2014). In this section, we illustrate the modelled results of the Orszag-Tang vortex flow. We simulate the Orszag-Tang vortex flow by the ERK2 described in Eq. (20) and the the pseudo-time marching method (P-t) described in Subsection 3.3, respectively.

The computational domain of the Orszag-Tang vortex system is set as $[0, 2\pi] \times [0, 2\pi]$, and the periodic boundary condition is implemented in both x and y directions. The initial state is given below.

$$\rho(x,y) = \gamma^2, \quad u(x,y) = -\sin y,$$
$$v(x,y) = \sin x, \quad w(x,y) = 0,$$
$$p(x,y) = \gamma, \quad B_x(x,y) = -\sin y,$$
$$B_y(x,y) = \sin 2x, \quad B_z(x,y) = 0,$$

with $\gamma = \frac{5}{3}$. In the Orszag-Tang vortex simulation, the time-step size is described as $\Delta t = \text{CFL} \cdot \min_{\forall \text{cell } i} \frac{\Delta h_i}{\max_{\forall \text{faces}} (|v_n| + c_f)}$. The grid resolution of the Orszag-Tang vortex flow modeled by the ERK2 scheme is 400×400, and CFL is set to be 0.5. As for the Orszag-Tang vortex flow modeled by the P-t method, we adopt grid resolutions of 400×400 and 800×800 and set CFL to 4 and 8, respectively. During the simulation, the physical time steps are around 3×10^{-3} for the test modeled by the ERK2 scheme and 1.2×10^{-2} for the tests modeled by the P-t method. Since Δt is not too large and the matrix $\left(\frac{\partial \mathbf{R}'}{\partial \mathbf{U}}\right)^{n+1,m}$ in Eq. (18) doesn't change obviously in the P-t iterations of a physical time step, we modify Eq. (18) as bellow, inspired by the Jacobian recycling strategies proposed in Persson (2013) and Zahr & Persson (2013), to reduce the computation cost.

$$\left(\frac{V}{\Delta\tau}\mathbf{I} + \frac{V}{\Delta t}\mathbf{I} + \left(\frac{\partial \mathbf{R}'}{\partial \mathbf{U}}\right)^{n+1,0}\right)\Delta\mathbf{U}^{n+1,m} = \frac{V}{\Delta t}\left(\mathbf{U}^n - \mathbf{U}^{n+1,m}\right) - \mathbf{R}^{n+1,m}$$

(A.1)

Thesemodeledd results are demonstrated as follows. In Fig. A.1, the contour images of density and thermal pressure of the Orszag-Tang vortex flow at $t = 3$, modeled by the ERK2 scheme with a resolution of 400×400 grid cells, and modeled by the P-t method with resolutions of 400×400 grid cells and 800×800 grid cells, are illustrated. The CFL number of the physical time step is set to be 0.5, 2, and 4, respectively. All these flow fields evolve in symmetrical patterns, and more detailed structures of low density are identified by the P-t method with the refined mesh. In Fig. A.2, we compare the density and thermal pressure profiles along the $y = 0.625\pi$ line at $t = 3$. It shows that shock discontinuities are formed around $x = 0.5$, $x = 1.6$, and $x = 4.4$ for all these three tests, and the shock discontinuities modeled by P-t method with the refined mesh are sharper than those modeled by the ERK2 scheme with coarse mesh.

It can be seen that these model results conform to the previous simulations (Balsara 2010; Feng et al. 2019; Fuchs et al. 2009; Jiang et al. 2010; Yang et al. 2017), demonstrating that the implicit LU-SGS method and pseudo-time marching method used in this solar coronal model can also be used to simulate small-scale unsteady flows accurately. Therefore, the MHD coronal model proposed in this paper is very promising. It

can perform high-fidelity simulations of critical but small-scale physics phenomena, such as transition region dynamics, and investigate their effects on the corona (Caplan et al. 2017).

Appendix B: Data communication between different components

To improve the precision of data communication, we transfer the reconstructed formulation of variables, not just the point values, between adjacent processors whose grid meshes share some overlapping area. As illustrated in Fig. B.1, we first derive the reconstruction formulation of a variable in the ghost cell of the blue component, the centroid of this ghost cell is denoted by P, from the stencil in red component, and then send this reconstruction formulation to the blue component to provide solution information in the ghost cell of this blue component.

During this data communication procedure, we first search the cell centroid P', which is closest to P in the component with red grids. The cell P' with centroid denoted by P' and its six neighboring cells which share an interface with cell P' serve as a stencil. We implement the RBF interpolation method (Liu et al. 2016; Wang et al. 2022a) to calculate the variable at point P. Afterward, we calculate a second-order Taylor polynomial expanding from P in the component with red grids by employing a least-square (LSQ) method (Barth 1991, 1993), and the stencil consists of point P, cell P' and cell P''s six neighboring cells which share an interface with it. Finally, the second-order Taylor polynomial derived from the red component is sent to the blue component to maintain synchronization of this blue component's ghost and inner cells. This synchronized MPI data communication is implemented before each LU-SGS iteration in the quasi-steady coronal simulations and time-dependent CME simulations to help maintain the synchronization of each processor's ghost cells and inner cells.

References

Abbo, L., Lionello, R., Riley, P., & Wang, Y. M. 2015, Sol. Phys., 290, 2043
Abramenko, V., Yurchyshyn, V., Linker, J. A., et al. 2010, ApJ, 712, 813
Arge, C., Luhmann, J., Odstrcil, D., Schrijver, C., & Li, Y. 2004, J. Atmos. Sol.-Terr. Phys., 66, 1295
Arge, C. N., Odstrcil, D., Pizzo, V. J., & Mayer, L. R. 2003, AIP Conf. Proc., 679, 190
Baker, D. N. 1998, Adv. Space Res, 22, 7
Balsara, D. S. 2010, J. Comput. Phys., 229, 1970
Barth, T. J. 1991, in 10th Computational Fluid Dynamics Conference, 24 June 1991-26 June 1991, Honolulu, HI, U.S.A., aIAA 1991-1548
Barth, T. J. 1993, in 31st Aerospace Sciences Meeting, aIAA 1993-668
Barth, T. J. & Jespersen, D. C. 1989, in 27th Aerospace Sciences Meeting, aIAA 1989-0366
Bijl, H., Carpenter, M. H., Vatsa, V. N., & Kennedy, C. A. 2002, J. Comput. Phys., 179, 313
Bourdin, P.-A. 2017, ApJL, 850, L29
Brchnelova, M., Kuźma, B., Perri, B., Lani, A., & Poedts, S. 2022, ApJS, 263, 18
Brchnelova, M., Kuźma, B., Zhang, F., Lani, A., & Poedts, S. 2023, A & A, 676
Brueckner, G. E., Howard, R. A., Koomen, M. J., et al. 1995, Sol. Phys., 162, 357
Burlaga, L. F., Sittler, E. C., Mariani, F., & Schwenn, R. 1981, J. Geophys. Res.: Space Phys., 86, 6673
Caplan, R. M., Linker, J. A., Mikić, Z., et al. 2019, J. Phys.: Conf. Ser., 1225, 012012
Caplan, R. M., Mikić, Z., Linker, J. A., & Lionello, R. 2017, J. Phys.: Conf. Ser., 837, 012016
Chen, P. F. 2011, Living Rev. Sol. Phys., 8, 1
Cheng, X., Guo, Y., & Ding, M. 2017, Sci. China Earth Sci., 60
Cheung, M. C. M. & DeRosa, M. L. 2012, ApJ, 757, 147
Detman, T., Smith, Z., Dryer, M., et al. 2006, J. Geophys. Res.: Space Phys., 111, A07102
Dryer, M. 2007, Asian J. Phys., 16, 97
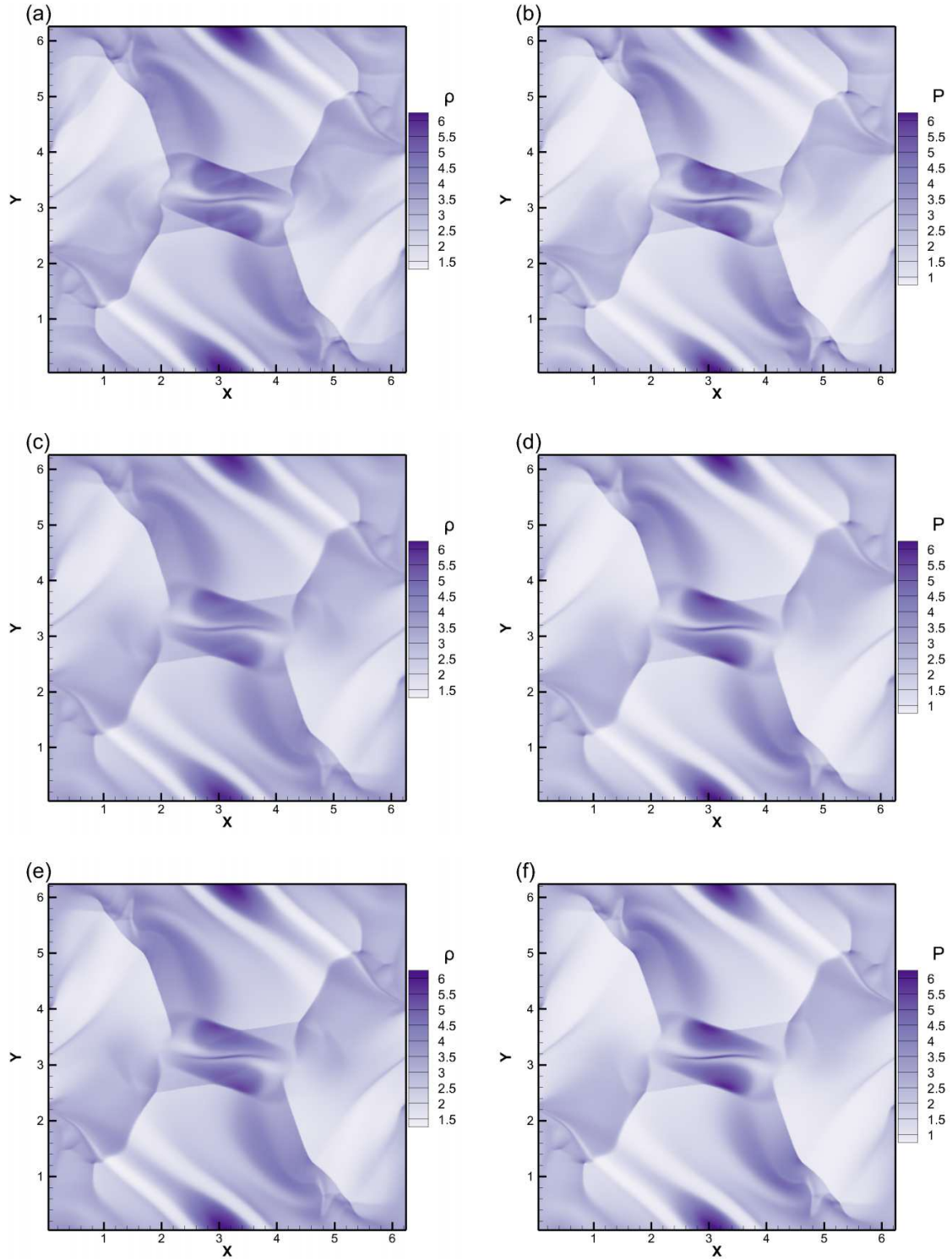
Fig. A.1. The contours of density (a, c, and e) and thermal pressure (b, d, and f) for MHD vortex problem at $t = 3$, modeled by ERK2 with 400×400 grids (a, b), by P-t with 400×400 grids (c, d), and by P-t with 800×800 grids (e, f), respectively.

Einfeldt, B., Munz, C. D., Roe, P. L., & Sjogreen, B. 1991, J. Comput. Phys., 92, 273

Endeve, E., Leer, E., & Holzer, T. E. 2003, ApJ, 589, 1040

Feng, X. S. 2020a, in Magnetohydrodynamic Modeling of the Solar Corona and Heliosphere, 125–337

Feng, X. S. 2020b, Magnetohydrodynamic Modeling of the Solar Corona and Heliosphere (Singapore: Springer)

Feng, X. S., Jiang, C. W., Xiang, C. Q., Zhao, X. P., & Wu, S. T. 2012a, ApJ, 758, 62

Feng, X. S., Li, C. X., Xiang, C. Q., et al. 2017, ApJS, 233, 10

Feng, X. S., Liu, X. J., Xiang, C. Q., Li, H. C., & Wei, F. S. 2019, ApJ, 871, 226

Feng, X. S., Ma, X. P., & Xiang, C. Q. 2015, J. Geophys. Res.: Space Phys., 120, 10,159

Feng, X. S., Wang, H. P., Xiang, C. Q., et al. 2021, ApJS, 257, 34

Feng, X. S., Xiang, C. Q., & Zhong, D. K. 2011a, Sci Sin-Terrae, 41, 1

Feng, X. S., Xiang, C. Q., & Zhong, D. K. 2013, Sci Sin-Terrae, 43, 912

Feng, X. S., Xiang, C. Q., Zhong, D. K., et al. 2014a, Comput. Phys. Commun, 185, 1965
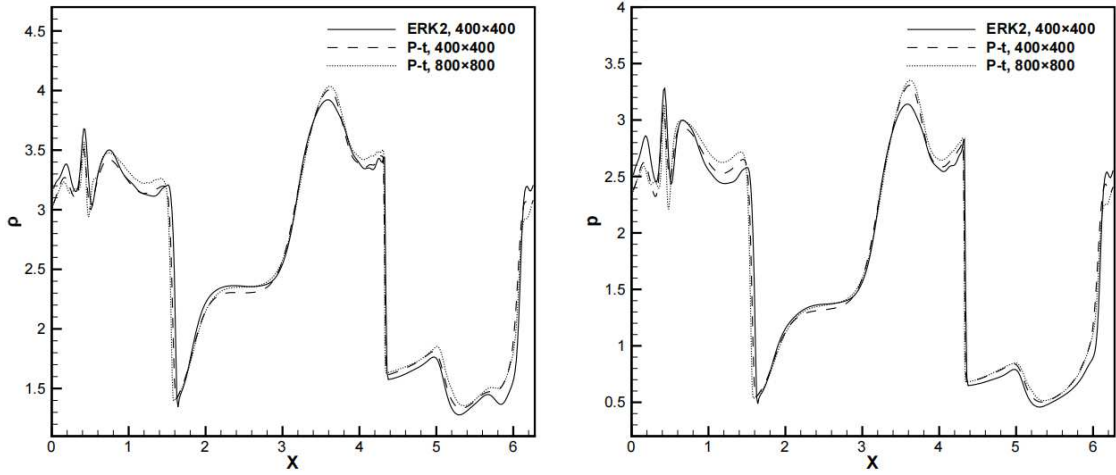
Fig. A.2. Profiles of density (left) and thermal pressure (right) at time $t = 3$ for the MHD vortex problem along line $y = 0.625\pi$, modeled by ERK2 with 400×400 grids (solid lines), by P-t with 400×400 grids (dashed lines), and by P-t with 800×800 grids (dotted lines), respectively.
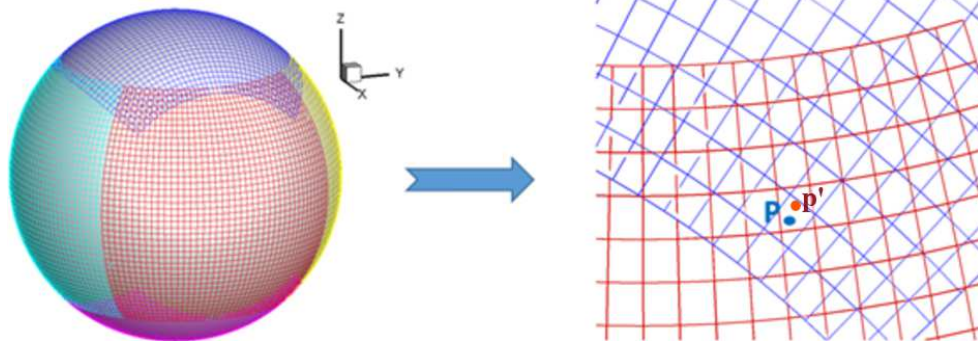
Fig. B.1. Illustration of the data communication between different components. The point denoted by P is a centroid of the ghost cell of the component with blue grids and is also in the computation domain of an adjacent component with red grids. The point denoted by P$'$ is the centroid of the cell closest to P in the component with red grids. The reconstruction formulation of a variable is first calculated in the stencil centered on a cell with its centroid denoted by P$'$ in the component with red grids and then transferred to the ghost cell with its centroid denoted by P in the component with blue grids.

Feng, X. S., Yang, L. P., Xiang, C. Q., et al. 2012b, Sol. Phys, 279, 207
Feng, X. S., Yang, L. P., Xiang, C. Q., et al. 2010, ApJ, 723, 300
Feng, X. S., Zhang, M., & Zhou, Y. F. 2014b, ApJS, 214, 6
Feng, X. S., Zhang, S. H., Xiang, C. Q., et al. 2011b, ApJ, 734, 50
Feng, X. S., Zhou, Y. F., & Wu, S. T. 2007, ApJ, 655, 1110
Fränz, M. & Harper, D. 2002, Planet. Space Sci, 50, 217
Frazin, R. A., Vásquez, A. M., Kamalabadi, F., & Park, H. 2007, ApJ, 671, 201
Fuchs, F. G., McMurry, A. D., Mishra, S., Risebro, N. H., & Waagan, K. 2010, J. Comput. Phys., 229, 4033
Fuchs, F. G., Mishra, S., & Risebro, N. H. 2009, J. Comput. Phys., 228, 641
Gibson, S. E. & Low, B. C. 1998, ApJ, 493, 460
Godunov, S. K. 1959, Mat. Sb. (N.S.), 1959,, 271
Gombosi, T. I., Van der Holst, B., Manchester, W. B., & Sokolov, I. V. 2018, Living Rev. Sol. Phys., 15, 4
Goodrich, C., Sussman, A., Lyon, J., Shay, M., & Cassak, P. 2004, J. Atmos. Sol.-Terr. Phys., 66, 1469, towards an Integrated Model of the Space Weather System
Groth, C. P. T., De Zeeuw, D. L., Gombosi, T. I., & Powell, K. G. 2000, J. Geophys. Res.: Space Phys., 105, 25053
Guo, J. H., Linan, L., Poedts, S., et al. 2023, A & A
Guo, J. H., Ni, Y. W., Qiu, Y., et al. 2021, ApJ, 917, 81
Guo, J. H., Ni, Y. W., Zhong, Z., et al. 2023, ApJS, 266, 3
Guo, X. C. 2015, J. Comput. Phys., 290, 352
Guo, Y., Cheng, X., & Ding, M. 2017, Sci. China Earth Sci., 60
Guo, Y., Xia, C., Keppens, R., & Valori, G. 2016, ApJ, 828, 82
Guo, Y., Xu, Y., Ding, M. D., et al. 2019, ApJL, 884, L1
Hamada, A., Asikainen, T., Virtanen, I., & Mursula, K. 2018, Sol. Phys., 293, 71
Hayashi, K., Abbett, W. P., Cheung, M. C. M., & Fisher, G. H. 2021, ApJS, 254, 1

Hayashi, K., Benevolenskaya, E., Hoeksema, T., Liu, Y., & Zhao, X. P. 2006a, ApJ, 636, L165
Hayashi, K., Zhao, X. P., & Liu, Y. 2006b, Geophys. Res. Lett., 33
Hayes, A. P., Vourlidas, A., & Howard, R. A. 2001, ApJ, 548, 1081
Hoeksema, J. T., Abbett, W. P., Bercik, D. J., et al. 2020, ApJS, 250, 28
Hollweg, J. V. 1978, Rev. Geophys., 16, 689
Hoshyari, S., Mirzaee, E., & Ollivier-Gooch, C. 2020, AIAA J., 58, 1490
Howard, R. A., Moses, J. D., Vourlidas, A., et al. 2008, Space Sci. Rev., 136, 67
Jiang, C. W., Feng, X. S., Zhang, J., & Zhong, D. K. 2010, Sol. Phys., 267, 463
Jiang, C. W., Wu, S. T., Feng, X. S., & Hu, Q. 2016, Nat. Commun., 7
Jiang, G.-S. & Wu, C.-C. 1999, J. Comput. Phys., 150, 561
Jin, M., Manchester, W. B., van der Holst, B., et al. 2017, ApJ, 834, 173
Kaiser, M. L., Kucera, T. A., Davila, J. M., et al. 2008, Space Sci. Rev., 136, 5
Kataoka, R., Ebisuzaki, T., Kusano, K., et al. 2009, J. Geophys. Res.: Space Phys., 114
Keppens, R., Braileanu, B. P., Zhou, Y. H., et al. 2023, A & A, 673
Koskinen, H. E. J., Baker, D. N., Balogh, A., et al. 2017, Space Sci. Rev, 212, 1137
Kuźma, B., Brchnelova, M., Perri, B., et al. 2023, ApJ, 942, 31
Lemen, J. R., Title, A. M., Akin, D. J., et al. 2012, Sol. Phys., 275, 17
Li, B., Habbal, S. R., Li, X., & Mountford, C. 2005, J. Geophys. Res.: Space Phys., 110
Li, H. C. & Feng, X. S. 2018, J. Geophys. Res.: Space Phys., 123, 4488
Li, H. C., Feng, X. S., & Wei, F. S. 2020, J. Space Weather Space Clim.
Li, H. C., Feng, X. S., & Wei, F. S. 2021, J. Geophys. Res.: Space Phys., 126, e2020JA028870
Li, L. Q., Lou, J. L., Luo, H., & Nishikawa, H. 2019, in AIAA Aviation 2019 Forum, aIAA 2019-3060

Li, W. A. & Ren, Y.-X. 2012, J. Comput. Phys., 231, 4053¡V4077

Li, W. A., Ren, Y.-X., Lei, G. D., & Luo, H. 2011, J. Comput. Phys., 230, 7775¡V7795

Li, W. N. & Ren, Y. X. 2012, Int. J. Numer. Methods Fluids, 70, 742

Linan, L., Regnault, F., Perri, B., et al. 2023, A & A, 675, A101

Linker, J. A., Mikić, Z., Biesecker, D. A., et al. 1999, J. Geophys. Res.: Space Phys., 104, 9809

Linker, J. A., Torok, T., Downs, C., et al. 2024, J. Phys.: Conf. Ser., 2742, 012012

Lionello, R., Linker, J. A., & Mikić, Z. 2008, ApJ, 690, 902

Liu, X. J., Feng, X. S., Zhang, M., & Zhao, J. M. 2023, ApJS, 265, 19

Liu, Y. L., Zhang, W. W., Jiang, Y. W., & Ye, Z. Y. 2016, Comput. Math. with Appl., 72, 1096

Ljubomir, N. & Larisa, T. 2012, IJGEE, 6, 698

Lugaz, N. & Roussev, I. 2011, J. Atmos. Sol.-Terr. Phys., 73, 1187, three dimensional aspects of CMEs, their source regions and interplanetary manifestations

Luo, H., Baum, J. D., & Löhner, R. 2001, Comput. Fluids, 30, 137

Marubashi, K., Cho, K., Kim, R.-S., et al. 2016, Earth Planets Space, 68

Mays, M., Taktakishvili, A., Pulkkinen, A., et al. 2015, Sol. Phys., 290

Mignone, A., Zanni, C., Tzeferacos, P., et al. 2011, ApJS, 198, 7

Mikić, Z., Linker, J. A., Schnack, D. D., Lionello, R., & Tarditi, A. 1999, Phys. Plasmas, 6, 2217

Nakamizo, A., Tanaka, T., Kubo, Y., et al. 2009, J. Geophys. Res.: Space Phys., 114

Newkirk, G., Dupree, R. G., & Schmhl, E. J. 1970, Sol. Phys., 15, 15

Nieves-Chinchilla, T., Linton, M. G., Hidalgo, M. A., & Vourlidas, A. 2018, ApJ, 861, 139

Noventa, G., Massa, F., Rebay, S., Bassi, F., & Ghidoni, A. 2020, Comput. Fluids, 204, 104529

Odstrcil, D. & Pizzo, V. J. 1999, J. Geophys. Res.: Space Phys., 104, 483

Odstrcil, D., Pizzo, V. J., Linker, J. A., et al. 2004, J. Atmos. Sol.-Terr. Phys., 66, 1311, towards an Integrated Model of the Space Weather System

Ogino, T. & Walker, R. J. 1984, Geophys. Res. Lett., 11, 1018

Orszag, S. A. & Tang, C.-M. 1979, J. Fluid Mech., 90, 129

Otero, E. & Eliasson, P. 2015a, Int J Comut Fluid Dyn, 29, 133

Otero, E. & Eliasson, P. 2015b, Int J Comut Fluid Dyn, 29, 313

Ouyang, Y., Zhou, Y. H., Chen, P. F., & Fang, C. 2017, ApJ, 835, 94

Owens, M. J., Lockwood, M., & Riley, P. 2017, Sci Rep, 7, 41548

Parker, E. N. 1963, Interplanetary dynamical processes (New York: Interscience Publishers)

Perri, B., Kuźma, B., Brchnelova, M., et al. 2023, ApJ, 943, 124

Perri, B., Leitner, P., Brchnelova, M., et al. 2022, ApJ, 936, 19

Persson, P.-O. 2013, J. Comput. Phys., 233, 414

Petrie, G. J. D., Canou, A., & Amari, T. 2011, Sol. Phys., 274, 163

Petrov, M. N., Titarev, V. A., Utyuzhnikov, S. V., & Chikitkin, A. V. 2017, Comput. Math. Math. Phys., 57, 1856

Poedts, S., Lani, A., Scolini, C., et al. 2020, J. Space Weather Space Clim., 10, 57

Pomoell, J. & Poedts, S. 2018, J. Space Weather Space Clim., 8, A35

Powell, K. G., Roe, P. L., Linde, T. J., Gombosi, T. I., & de Zeeuw, D. L. 1999, J. Comput. Phys., 154, 284

Priest, E. 2014, Magnetohydrodynamics of the Sun (Cambridge: Cambridge University Press), 144–176

Regnault, F., Strugarek, A., Janvier, M., et al. 2023, A & A, 670, A14

Reiss, M. A., MacNeice, P. J., Mays, L. M., et al. 2019, ApJS, 240, 35

Riley, P., Linker, J. A., Lionello, R., & Mikić, Z. 2012, J. Atmos. Sol.-Terr. Phys., 83, 1

Riley, P., Lionello, R., Linker, J. A., et al. 2015, ApJ, 802, 105

Riley, P., Lionello, R., Linker, J. A., et al. 2011, Sol. Phys., 274, 361

Samara, E., Pinto, R. F., Magdaleni, J., et al. 2021, A & A, 648, A35

Schatten, K. H., Wilcox, J. M., & Ness, N. F. 1969, Sol. Phys., 6, 442

Scolini, C., Rodriguez, L., Mierla, M., Pomoell, J., & Poedts, S. 2019, A & A, 626, A122

Sharov, D., Luo, H., Baum, J., & Loehner, R. 2000, in 38th Aerospace Sciences Meeting and Exhibit, aIAA 2000-927

Shen, F., Liu, Y. S., & Yang, Y. 2021, ApJS, 253, 12

Singer, H. J., Heckman, G. R., & Hirman, J. W. 2001, Space Weather Forecasting: A Grand Challenge (Washington, DC: American Geophysical Union (AGU)), 23–29

Singh, T., Yalim, M. S., Pogorelov, N. V., & Gopalswamy, N. 2020, ApJ, 894, 49

Siscoe, G. 2000, J. Atmos. Sol.-Terr. Phys., 62, 1223

Sitaraman, H. & Raja, L. L. 2013, J. Comput. Phys., 251, 364

Steinolfson, R. S. & Hundhausen, A. J. 1988, J. Geophys. Res.: Space Phys., 93, 14269

Suess, S., Wang, A.-H., & Wu, S. 1996, J. Geophys. Res.: Space Phys., 101, 19957

Sun, X., Liu, Y., Hoeksema, J. T., Hayashi, K., & Zhao, X. 2011, Sol. Phys., 270, 9

Tanaka, T. 1995, J. Geophys. Res.: Space Phys., 100, 12057

Thompson, W. & Reginald, N. 2008, Sol. Phys., 250, 443

Thompson, W. T. 2006, A & A, 449, 791

Thompson, W. T., Davila, J. M., Fisher, R. R., et al. 2003, in SPIE Astronomical Telescopes + Instrumentation

Titov, V. S., Downs, C., Mikić, Z., et al. 2017, ApJL, 852

Titov, V. S., Török, T., Mikić, Z., & Linker, J. A. 2014, ApJ, 790, 163

Török, T., Berger, M. A., & Kliem, B. 2010, A & A, 516, A49

Tóth, G. 2000, J. Comput. Phys., 161, 605

Tóth, G., van der Holst, B., Sokolov, I. V., et al. 2012, J. Comput. Phys., 231, 870

Usmanov, A. V. 1993, Sol. Phys., 146, 377

Usmanov, A. V. & Goldstein, M. L. 2003, AIP Conf. Proc., 679, 393

Vourlidas, A., Lynch, B., Howard, R., & Li, Y. 2012, Sol. Phys., 284

Vourlidas, A., Patsourakos, S., & Savani, N. P. 2019, Philos. Trans. R. Soc., A, 377, 20180096

Wang, H. P., Xiang, C. Q., Liu, X. J., Lv, J. K., & Shen, F. 2022a, ApJ, 935, 46

Wang, H. P., Zhao, J. M., Lv, J. K., & Liu, X. J. 2022b, Chin. J. Geophys., 65, 2779

Wang, Y., Feng, X. S., & Xiang, C. Q. 2019, Comput. Fluids, 179, 67

Wang, Y. M., N. R. Sheeley, J., & Rich, N. B. 2007, ApJ, 658, 1340

Wu, S. T. & Dryer, M. 2015, Sci. China Earth Sci., 58, 839

Wu, S. T., Guo, W. P., Michels, D. J., & Burlaga, L. F. 1999, J. Geophys. Res.: Space Phys., 104, 14789

Xia, C., Teunissen, J., Mellah, I. E., Chané, E., & Keppens, R. 2018, ApJS, 234

Xia, Y. D., Luo, H., & Nourgaliev, R. 2014, Comput. Fluids, 96, 406

Xu, Y., Zhu, J. H., & Guo, Y. 2020, ApJ, 892, 54

Yang, L. P., Feng, X. S., Xiang, C. Q., Zhang, S. H., & Wu, S. T. 2011, Sol. Phys., 271, 97

Yang, L. P., Wang, H. P., Feng, X. S., et al. 2021, ApJ, 918, 31

Yang, Y., Feng, X. S., & Jiang, C. W. 2017, J. Comput. Phys., 349, 561

Yang, Z. C., Shen, F., Yang, Y., & Feng, X. S. 2018, Chin. J. Space Sci., 38, 285

Zahr, M. J. & Persson, P.-O. 2013, in 21st AIAA Computational Fluid Dynamics Conference, June 24-27, 2013, San Diego, CA.

Zhang, J., Cheng, X., & Ding, M. 2012, Nat. Commun., 3, 747

Zhang, M., Feng, X. S., Li, H. C., et al. 2023, Front. astron. space sci., 10

Zhang, M., Feng, X. S., & Yang, L. P. 2019, J. Space Weather Space Clim., 9, A33

Zhang, M. J., John Yu, S. T., Henry Lin, S. C., Chang, S.-C., & Blankson, I. 2006, J. Comput. Phys., 214, 599

Zhao, X. P., Plunkett, S. P., & Liu, W. 2002, J. Geophys. Res.: Space Phys., 107, SSH 13

Zhou, Y. F. & Feng, X. S. 2014, Sci. China Earth Sci., 57, 153

Zhou, Y. F. & Feng, X. S. 2017, J. Geophys. Res.: Space Phys., 122, 1451

Zhou, Y. F., Feng, X. S., Wu, S. T., et al. 2012, J. Geophys. Res.: Space Phys., 117